ARTICLE IN PRESS

Available online at www.sciencedirect.com
ScienceDirect

Geochimica et Cosmochimica Acta xxx (2007) xxx–xxx

Geochimica et Cosmochimica Acta

www.elsevier.com/locate/gca

Chemical weathering in the Hong (Red) River basin: Rates of silicate weathering and their controlling factors

Seulgi Moon [a], Youngsook Huh [a,*], Jianhua Qin [b], Nguyen van Pho [c]

[a] *School of Earth and Environmental Sciences, Seoul National University, San 56-1, Sillim-dong, Gwanak-gu, Seoul 151-747, Republic of Korea*
[b] *Chengdu Institute of Geology and Mineral Resources, Chengdu, Sichuan 610082, PR China*
[c] *Institute of Geological Sciences, National Centre for Natural Sciences & Technology, Hanoi, Vietnam*

Received 12 June 2006; accepted in revised form 5 December 2006

Abstract

The Hong (Red) River drains the prominent Red River Fault Zone that has experienced various tectonic activities—intrusion of magma, exhumation of basement rocks, and influx of thermal waters—associated with the Cenozoic collision of India and Eurasia. We report dissolved major element and Sr isotope compositions of 43 samples from its three tributary systems (Da, Thao/Hong main channel, and Lo) encompassing summer and winter seasons. Carbonic acid ultimately derived from the atmosphere is the main weathering agent, and sulfuric acid from pyrite oxidation plays a minor role. Seasonality is manifested in higher calcite saturation index and Mg/TZ^{+} and lower Ca/Mg in summer, suggesting calcite precipitation, and in higher Si/(Na^{*} + K) ratios in summer suggesting more intensive silicate weathering. We quantified the input from rain, evaporite, carbonate, and silicate reservoirs using forward and inverse models and examined the robustness of the results. Carbonate dissolution accounts for a significant fraction of total dissolved cations (55–97%), and weathering of silicates makes a minor contribution (1–40%). Our best estimate of the spatially averaged silicate weathering rate in the Hong basin is 170×10^3 mol/km^2/yr in summer and 51×10^3 mol/km^2/yr in winter. We tested for correlations between the rate of CO_2 consumption by silicate weathering and various climatic (air temperature, precipitation, runoff, and potential evapotranspiration) and geologic (relief, elevation, slope, and lithology) parameters calculated using GIS. Clear correlations do not emerge (except for ϕCO_2 and runoff in winter) which we attribute to the complex geologic setting of the area, the seasonal regime change from physical-dominant in summer to chemical-dominant in winter, and the incoherent timescales involved for the different parameters tested.
© 2006 Elsevier Inc. All rights reserved.

1. INTRODUCTION

Chemical weathering of silicate rocks acts as a net sink for atmospheric CO_2 over >1 m.y., and climatic and geologic factors controlling its rate and feedback mechanisms have attracted much interest as regulators of atmospheric CO_2 levels over geologic timescales (Walker et al., 1981; Berner, 1991; Edmond, 1992; Raymo and Ruddiman, 1992). Walker et al. (1981) proposed that the temperature-dependence of silicate weathering rates constitutes a negative feedback on atmospheric CO_2. Raymo and Ruddiman (1992) countered by ascribing the Cenozoic deterioration in global climate to the rise of the Himalayas and the resulting increase in mechanical and chemical weathering rates and consumption of atmospheric CO_2. In order to test the former "thermostat" hypothesis or the latter "uplift-weathering" hypothesis, we require field data on chemical weathering rates under various climatic and geologic conditions. Hitherto, rivers draining the Himalayas have been the focus because of the high chemical weathering rates, unusually high delivery of radiogenic Sr, and temporal association between the rise of the Himalayas and the Cenozoic global cooling (Raymo and Ruddiman, 1992; Galy et al., 1999; Krishnaswami et al., 1999). Recognizing the

* Corresponding author. Fax: +82 2 871 3269.
E-mail address: yhuh@snu.ac.kr (Y. Huh).

0016-7037/$ - see front matter © 2006 Elsevier Inc. All rights reserved.
doi:10.1016/j.gca.2006.12.004

importance of the Tibetan Plateau as a prominent topographic and tectonic feature in the area and in the generation of the Asian monsoon system, we extended our study of riverine geochemistry to the Hong (Red) River in the eastern periphery of the Tibetan Plateau.

Quantification of silicate weathering rates from field studies of large rivers involves applying models and proxies to calculate the amount of major elements and isotopes from various potential sources—rain, evaporite, carbonate, silicate, sulfide, and anthropogenic input (Gaillardet et al., 1999; Krishnaswami et al., 1999; Bickle et al., 2005). The 'forward' and 'inverse' models both consist of mass balance equations involving cations (Na, Ca, Mg, and K) and make *a priori* assumptions about the compositions of the pre-assigned source reservoirs. For both models, the uncertainties are ultimately dependent on the ability to correctly define the relevant reservoirs and to assign appropriate end member constraints (Négrel et al., 1993; Wu et al., 2005).

Deriving a functional relationship between silicate weathering rates and their controls, such as climatic (temperature, precipitation, runoff, and potential evapotranspiration) and geologic (relief, elevation, slope, and lithology) factors (Gaillardet et al., 1999; Millot et al., 2003; West et al., 2005) in present-day environments is important for applying the underlying relationship to interpreting paleorecords or for implementing into global carbon cycle models. Recent development in remote sensing and GIS-based digital data processing tools enables numerical analyses of climatic and geologic parameters at basin scales and provides us with a tool to quantify the potential agents in chemical weathering.

We analyzed the major element and Sr isotopic composition of the Hong River in south China and north Vietnam. Rates of silicate weathering and CO_2 uptake are quantified and then correlations with climate (runoff, precipitation, air temperature, and potential evapotranspiration) and geology (relief, elevation, slope, and surface rock portion) examined. Spatial variation in the three tributary systems and temporal variation between summer and winter are also investigated.

2. STUDY AREA

2.1. Geography, vegetation, and climate

The Hong hails from southeast of the Tibetan Plateau in the Yunnan Province, China and flows along the NW–SE trending Red River Fault Zone to the Gulf of Tonkin in the South China Sea. The name originates from the large quantity of silt, rich in iron oxide, that the river carries (Penn, 2001). The drainage area of the Hong is 157×10^3 km^2 (Wolf et al., 1999) of which our study area covers ~86% (Fig. 1). The samples are organized into three groups according to the three major tributaries—the Da, Thao (Hong main channel), and Lo—occupying 38%, 35%, and 27% of the study area, respectively.

The Hong drainage basin is in a subtropical monsoon climate regime, and the temperature, precipitation, evaporation, and runoff undergo seasonal fluctuations. Average air temperature over the Hong drainage basin varies from 12 °C in winter to 22 °C in summer, monthly precipitation from 18 (winter) to 210 (summer) mm, and potential evapotranspiration (PET) from 58 (winter) to 100 (summer) mm (Fig. 2 and Table 1). Vegetation is mainly tropical to subtropical moist broadleaf forest with local subtropical coniferous forest above 22–23°N (World Wildlife Fund, 2000). Total water discharge of the Hong is ~120 km^3/yr (32nd in the world), and average suspended sediment transport is $\sim 130 \times 10^6$ t/yr (14th in the world) (Meybeck and Ragu, 1997). Water discharge in Hanoi is highest (725 km^3/yr) in July and August and lowest (22 km^3/yr) in January–March (Mathers and Zalasiewicz, 1999). During the summer monsoon season, the suspended sediment concentration is ~12 g/l and accounts for up to 90% of annual sediment load (Mathers et al., 1997; Mathers and Zalasiewicz, 1999).

2.2. Tectonics and geology

The Tibetan Plateau is ~2000 km wide and its average elevation is ~5 km. Eastward extrusion of the Indochina block from the Tibetan Plateau formed the NW–SE trending Red River Fault Zone (RRFZ), a great right lateral fault following a series of narrow high-grade gneiss ranges (Schärer et al., 1990; Leloup et al., 1995; Zhang and Schärer, 1999) (Fig. 1b). The RRFZ is the southeastern member of the larger NW-WNW trending Red River-Jinshajiang fault zone linking the Red River area to the Yangtze headwaters in Tibet.

Two continental blocks meet in the Hong basin: the South China block (Yangtze Platform) and the Indochina block (Fig. 1b). Ophiolites of the Song Ma suture zone mark the boundary between the two blocks which were sutured ~250 Ma (Lan et al., 2001). Along the Thao/Hong main channel, metamorphic gneiss (2.3–1.0 Ga) with sillimanite-mica schist and amphibolite is exposed (Lan et al., 2001). Between the RRFZ and the Song Ma suture zone are found Mid-Proterozoic to Early Cenozoic age igneous rock suites of calc-alkaline to high K calc-alkaline granites (Lan et al., 2000).

The headwaters of the Thao drains the Chuxiong Basin composed of thick Upper Triassic to Lower Cenozoic sequences of coal-bearing continental clastic rocks (Leloup et al., 1995; Burchfiel and Wang, 2003; Wang et al., 2005). Mafic and ultramafic intrusions hosting sulfide deposits are also exposed along the RRFZ (Wang et al., 2005) (Fig. 1). The Da drains the Yangbi and Simao basins with Paleozoic and Mesozoic cover of continental red beds and, close to the RRFZ, Permo-Carboniferous limestones (Leloup et al., 1995). Felsic and ultramafic rocks are limited to a few scattered exposures near the RRFZ. The Lo drains the South China Fold Belt, which is characterized by a thick marine succession of Triassic limestone and fine-grained clastic rocks (Burchfiel and Wang, 2003) (Fig. 1b). Between the Lo main channel and the Chay tributary, Proterozoic to Lower Paleozoic low-grade metamorphic and sedimentary rocks are exposed along with small granitoid intrusions (Wysocka and Swierczewska, 2003) (Fig. 1b).

In summary, the three main tributaries of the Red River drainage system have considerable differences in their

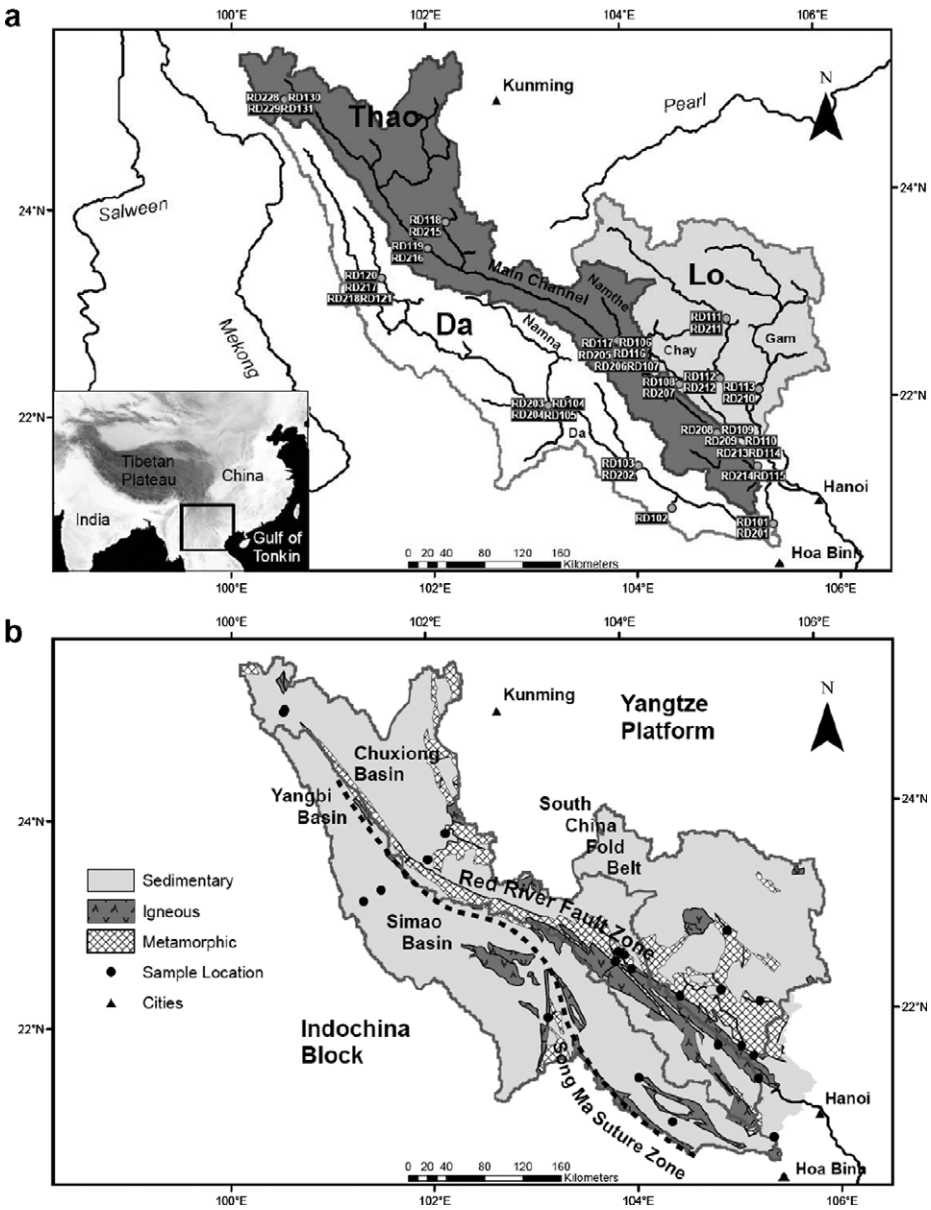

Fig. 1. (a) Sample location map of the Hong (Red) River with the three sub-basins of the Da, Thao (Hong main channel), and Lo delineated. (b) Geologic map modified from the digital map of east and southeast Asia (Wakita et al., 2004). The rock type is divided into 3 categories—sedimentary, igneous (including volcanic, plutonic, and ultramafic), and metamorphic. The thick dashed line indicates the boundary between the Yangtze Platform and the Indochina block.

lithologies. The Thao is dominated by metamorphic rocks, except in the upper reaches with coal-bearing sedimentary deposits and sulfide-bearing ultramafic intrusions. The Da drainage is composed of sedimentary rocks of Mesozoic and Paleozoic age with minor felsic intrusions. The Lo drainage has low-grade metamorphic rocks and Proterozoic to Paleozoic sedimentary rocks with some granitoid intrusions.

3. METHODOLOGY

River water samples were collected in summer from August to September 2001 and in winter from December 2002 to January 2003. Samples for major ions were filtered through 0.45 μm Millipore® filters and those for Sr through 0.4 μm polycarbonate filters in a portable laboratory in the field within 24 h of collection. The trace element samples and small aliquots for nutrient analyses were acidified with ultrapure HCl or HNO_3 and stored in HDPE bottles. The pH was measured at the sampling sites to ensure against CO_2 loss. Upon returning to the laboratory at Northwestern University, the major cations (K, Na, Ca, and Mg) were analyzed by flame atomic absorption spectrometry, alkalinity by Gran titration, Cl and SO_4 by ion chromatography, and Si (on acidified samples) by colorimetry. Strontium concentrations were determined by ICP-MS at

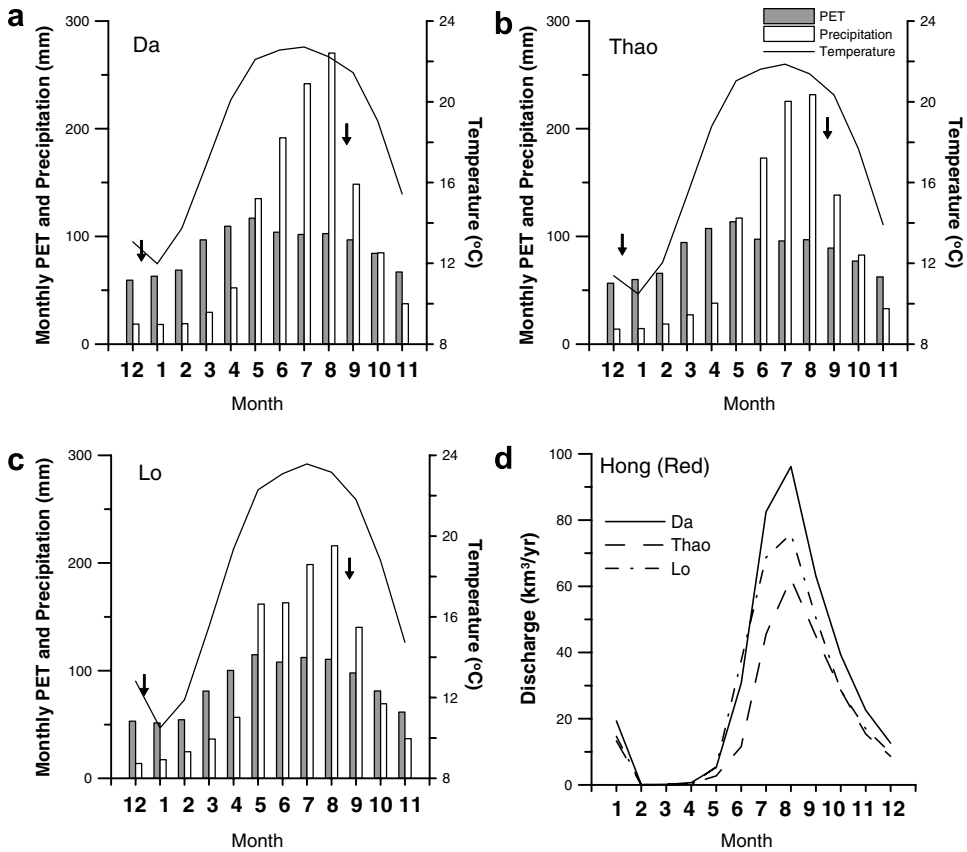

Fig. 2. Monthly variations of temperature, precipitation, and potential evapotranspiration (PET) at the furthest downstream sampling locations of the (a) Da (RD101), (b) Thao (RD115), and (c) Lo (RD114). (d) Water discharge at the three locations of a, b, and c. See text for data sources. Arrows indicate our sampling periods in winter and summer.

Northwestern University and the isotopic composition by TIMS at US Geological Survey, Menlo Park, CA. The long-term value for NBS987 was 0.71023 ± 0.00002.

The calcite and dolomite saturation indices (CSI, DSI) and the CO_2 partial pressure (pCO_2) were calculated with the Geochemist's Workbench® v.4.0 (Bethke, 2002) and the thermodynamic database provided with the program. Stepwise multiple regression and various statistical analyses were carried out with the SPSS® v.12.0 package. For the inverse model iterations, we used the commercial Premium Solver® optimization package with the Microsoft Excel® spreadsheet program.

We used ArcGIS® v.9 software to calculate the GIS parameters (Table 1). Climatic data (air temperature, precipitation, and evapotranspiration) were from Leemans and Cramer (1991), and runoff data were from the UNEP/GRDC composite Runoff Fields v 1.0 with 30 min resolution (Fekete et al., 2002). Drainage basin area was modified from the Hydro1k database for Asia obtained from the Land Processes Distributed Active Archive Center (LP DAAC) of USGS. The mean local relief ('maximum–minimum' elevation) was calculated from the 10-min gridded modal height data for land masses provided by the US Navy Fleet Numerical Oceanography Center (FNOC). This spatial resolution is equivalent to ~17 km at the 21–25°N latitude of the Hong drainage basin. The digital elevation model (DEM) was acquired from the 3-arc-s elevation data set from the Shuttle Radar Topography Mission (STRM), and the slope was calculated from the same dataset. Using the digital geologic map of east and southeast Asia (Wakita et al., 2004), we simplified the distribution of rock types as sedimentary, igneous (volcanic and ultramafic), and metamorphic rocks (Fig. 1b), and the sum of igneous and metamorphic rocks was grouped into non-sedimentary rocks (Table 1). Further subdivision of sedimentary rocks into clastic versus carbonate rocks would be most useful, but such information was not available at the spatial scale required for our study in a quantitative format. Population density was from LandScan Global Population 2000 Database developed by Oak Ridge National Laboratory (ORNL) with 30 min resolution (Hearn et al., 2001) (Table 1).

4. RESULTS AND DISCUSSION

4.1. Major elements

The pH was mildly alkaline—from 7.44 (RD201) to 8.51 (RD118), averaging 8.0. It was more alkaline in summer (8.20) than in winter (7.93), with seasonal contrast in the

ARTICLE IN PRESS

Table 1
Climatic and geologic parameters calculated from digital data sets (see Section 3)

Sample No.	Climatic (monthly)								Geologic					Population density indiv./km^2
	Temperature		Precipitation		Runoff		PET[a]		Relief (m)	Elevation (m)	Slope (deg)	Lithology (%)		
	Sum	Win	Sum	Win	Sum	Win	Sum	Win				Sed.	Non-sed.[b]	
Da														
RD120	19.8	9.8	192	17	105	22	90	61	1328	1555	19.9	91	9	46
RD121	19.0	8.9	182	15	116	27	87	60	1027	1698	20.7	98	2	56
RD105	20.4	10.8	202	19	118	25	95	62	1068	1334	20.9	94	6	39
RD104	21.3	12.1	180	17	109	21	100	60	1180	1252	22.9	78	22	56
RD103	21.2	11.9	200	18	129	26	98	61	1154	1219	21.0	89	11	40
RD102	25.1	—	261	—	124	—	103	—	694	939	16.6	87	13	55
RD101	21.8	12.5	208	18	130	26	99	61	1133	1147	20.6	87	13	44
Thao														
RD131	18.1	7.2	168	9	108	28	78	57	677	2029	14.4	89	11	248
RD130	18.0	7.2	163	10	95	26	79	57	852	2079	16.4	89	11	159
RD119	18.3	8.0	172	12	82	18	83	58	849	1789	18.6	86	14	75
RD118	18.9	9.2	171	15	43	6	89	58	760	1694	17.6	53	47	46
RD106	18.9	8.9	171	14	77	16	87	58	955	1642	19.2	72	28	73
RD117	20.0	—	150	—	92	—	98	—	895	1421	20.4	90	10	60
RD116	21.5	—	168	—	128	—	103	—	1163	891	20.1	88	12	44
RD107	20.4	10.7	155	15	101	20	99	55	962	1249	19.8	79	21	59
RD109	20.0	10.0	177	14	91	19	91	58	1008	1484	19.3	70	30	70
RD115	20.5	10.5	183	14	94	19	93	58	977	1390	18.8	69	31	80
Lo														
RD111	20.2	9.9	151	15	103	20	98	52	653	1527	13.8	91	9	109
RD112	24.1	13.8	198	15	165	34	108	56	1252	560	17.8	67	33	60
RD113	23.0	11.5	181	16	154	28	105	50	716	906	19.4	95	5	52
RD108	22.3	12.2	177	15	146	31	105	56	1103	1050	18.8	60	40	77
RD110	23.4	13.3	192	15	150	31	106	56	962	787	16.7	46	54	91
RD114	22.7	11.9	181	16	145	28	104	52	788	934	17.1	76	24	80

Furthest downstream samples in each tributary system are shaded.
—: no sample.
[a] PET means potential evapotranspiration.
[b] Non-sed.: non-sedimentary = igneous + metamorphic.

Please cite this article in press as: Moon S. et al., Chemical weathering in the Hong (Red) River basin: Rates ..., *Geochim. Cosmochim. Acta* (2007), doi:10.1016/j.gca.2006.12.004

Thao (0.39) and Da (0.33) but none in the Lo. The water temperatures measured at sample collection were 20.8–31.2 °C in summer and 9.6–20.2 °C in winter. The total dissolved cations ($TZ^+ = Na^+ + K^+ + 2Mg^{2+} + 2Ca^{2+}$) and total dissolved anions ($TZ^- = Cl^- + 2SO_4^{2-} + HCO_3^-$) were well balanced: 39 of the 43 samples had normalized inorganic charge balance, $NICB = (TZ^+–TZ^-)/TZ^+$, below 7%, and all samples had NICB <10% (Table 2).

Water discharge of the Hong River was 5 times higher during the summer sampling period (66 km^3/yr) than in winter (13 km^3/yr). A paired-samples *t*-test showed insignificant seasonal difference ($p = 0.052$) in the TDS (total dissolved solids): 70–244 mg/l (mean 172 mg/l) in summer and 76–338 mg/l (mean 179 mg/l) in winter. Only in the Da was there a decrease of ~15% in TDS ($p = 0.004$). Rivers in general do not undergo simple dilution in their dissolved chemical concentrations with increasing water discharge. Carbonate weathering tends to increase with runoff, whereas silicate-derived ions can undergo dilution above some threshold runoff (Stallard and Edmond, 1987; Berner and Berner, 1996). In one unusual sample, the Huanien He of the Thao (RD118), TDS increased 58% in summer despite the 10 times higher water discharge. We suspect this was due to the seasonal change in water flow path. The river normally drains a small area of igneous and metamorphic rocks, but in summer the areas underlain by sedimentary rocks may also be incorporated into the drainage.

The average TDS of the Hong was relatively high and similar to the Ganges (187 mg/l) and Indus (164 mg/l) draining the Himalayas and the Mackenzie draining the Rockies (160 mg/l) but was lower than the Upper Huang He (Yellow) (274 mg/l) (Karim and Veizer, 2000; Dalai et al., 2002; Millot et al., 2003; Wu et al., 2005). Other rivers draining orogenic zones have moderate TDS, e.g., the Brahmaputra draining the Himalayas and Tibetan Plateau (71 mg/l), the Amazon (41 mg/l) and Orinoco (82 mg/l) draining the Andes, or the rivers of the Russian Far East draining the collision zone (70 mg/l) (Edmond et al., 1996; Huh et al., 1998; Galy and France-Lanord, 1999; Dosseto et al., 2006). In comparison, rivers draining shield terrains have lower TDS—e.g., the Amazon draining the Brazilian Shield (11 mg/l), Orinoco draining the Guayana Shield (9 mg/l), St. Lawrence draining the Canadian Shield (32 mg/l), or the rivers draining the Siberian Shield (90 mg/l) (Edmond et al., 1995; Gaillardet et al., 1995; Gaillardet et al., 1997; Huh and Edmond, 1999; Millot et al., 2003).

Major cation concentrations were in the order of Ca > Mg > Na > K (on molar basis) (Table 2 and Fig. 3a). Ca concentrations were on average 11% lower and Mg 10% higher in summer. In the RD118 sample mentioned above, Ca, Mg, and Si were ~60%, 100%, and 60% higher in summer than in winter, respectively. Seasonal variation is discussed further in Section 4.3.4. Bicarbonate was the most abundant anion and made up more than 70% of TZ^- in charge equivalent units (Fig. 3b). Concentrations of Si varied from 96 to 246 μM (average 178 μM) and did not differ significantly among the three tributary systems ($p = 0.31$). Concentrations of SO_4 and Cl, on the other hand, were 2–3 times higher in the Thao than in the other two tributary systems.

4.2. Comparison to global rivers

We compared our Hong River data ($n = 43$) with those of 60 large rivers in the world which we will refer to as 'Global Rivers' (Gaillardet et al., 1999). Na-normalized molar ratios were used to facilitate comparison for different water discharge and evaporation. Molar ratios of Ca/Na and Mg/Na did not show log-normal distribution (Shapiro–Wilk test for normality, $p < 0.05$) but were skewed toward higher ratios than the Global Rivers; Cl/Na ratios displayed a log-normal distribution (Fig. 4a, b, and c). Ca/Na and Mg/Na ratios were 3 times higher and Cl/Na ratios 0.4 times lower than the average Global Rivers, which we qualitatively interpret as dominance of carbonates rather than silicates or evaporites in supplying dissolved elements to the Hong. The strontium isotope ratios also showed a skewed distribution, but the range in values was similar to that of Global Rivers (Fig. 4d). Maximum $^{87}Sr/^{86}Sr$ was 0.7217 (RD212) and minimum 0.7085 (RD102), but 70% of the Hong samples clustered between 0.710 and 0.714 with no extremely radiogenic samples indicative of old, Rb-rich silicate weathering (>0.80) or extremely unradiogenic samples indicative of young, Rb-poor basalt weathering (0.702–0.706). Most samples had $^{87}Sr/^{86}Sr$ values more radiogenic than Phanerozoic marine carbonates (0.7065–0.709) (Burke et al., 1982).

Mixing of the three representative lithologies—carbonate, silicate, and evaporite—can be displayed on plots of Na-normalized molar ratios (Fig. 5). The Hong samples plotted closer to the carbonate end member than do Global Rivers, with the Thao closest to the silicate and/or evaporite end members and the Lo closest to the carbonate end member (Fig. 5a and c). Winter data plotted closer to silicate/evaporite end members than summer data (Fig. 5b and d).

4.3. Effect of different rock types

Dissolved major elements in rivers come from atmospheric precipitation, chemical weathering of rocks and sediments, and anthropogenic input. The population density of our study area was ~80 (40–250) indiv./km^2, which is lower than the average population density of China (123 indiv./km^2) or those of the Chang Jiang (214 indiv./km^2) and Huang He (156 indiv./km^2) drainage basins but is higher than those of the Amazon, Mackenzie, and Siberian rivers (<5 indiv./km^2) (CIESIN et al., 2004). To examine the effect of anthropogenic input, we tested for a statistical relationship between the population density and the fluvial yield of K, an element supplied in fertilizers and potentially affected by agriculture which is the main economic activity in the Hong drainage basin. High correlations ($r^2 = 0.608$ with $p < 0.001$ in winter; $r^2 = 0.302$ with $p = 0.007$ in summer) were biased by two pairs of samples (RD131/RD229, RD130/RD228) in the upper Thao which had high yields not only for K but also for Na, SO_4, and Cl and had high population densities (250 and 160 indiv./km^2, respectively). Excluding these samples, the correlation between K yield and population density was insignificant at 5% significance level. Dissolved reactive phosphorus (Wu and Huh, in review) and Cl, two other elements sensitive to human activ-

ARTICLE IN PRESS

Table 2
The dissolved chemical composition of the Hong River

Sample No.	Date yyyy-mm-dd	River name[a]	pH	T[b] (°C)	Na (μM)	K (μM)	Mg (μM)	Ca (μM)	Cl (μM)	SO_4 (μM)	Alk (μEq)	Si (μM)	TDS[c] (mg/l)	Sr (μM)	$^{87}Sr/^{86}Sr$	NICB[d] (%)
Da																
RD120	2001-09-07	Amo Jiang	8.38	24.4	104	19.5	201	591	23.9	55.5	1557	176	142	0.809	0.71363	0.9
RD217	2003-01-07	Amo Jiang	7.81	14.6	147	24.6	192	737	32.7	90.8	1880	123	169	1.112	0.71330	−3.2
RD121	2001-09-07	Babian Jiang	8.17	24.8	94.0	19.1	185	611	30.6	34.1	1590	150	141	0.677	0.71306	1.0
RD218	2003-01-07	Babian Jiang	7.75	17.0	165	16.2	242	989	64.9	71.2	1989	108	177	0.939	0.71249	2.1
RD105	2001-08-19	Da @ Lai Chau	8.23	27.1	129	20.7	145	455	28.7	33.2	1201	214	115	0.668	0.71365	3.9
RD203	2002-12-29	Da @ Lai Chau	7.83	20.2	146	19.2	127	572	25.6	49.0	1514	202	139	0.878	0.71321	−4.7
RD104	2001-08-19	Namna @ Lai Chau	8.14	26.8	104	28.8	135	418	12.2	39.9	1105	264	110	0.813	0.71159	3.4
RD204	2002-12-29	Namna @ Lai Chau	7.64	19.1	120	28.3	119	487	9.9	53.6	1313	247	125	1.192	0.71081	−5.2
RD103	2001-08-18	Da @ Muong La, ab res	8.14	31.2	106	24.4	163	525	16.1	39.0	1369	228	129	0.825	0.71213	2.9
RD202	2002-12-28	Da @ Muong La, ab res	8.03	18.1	119	25.7	119	533	15.6	53.6	1452	207	133	10.71	0.71127	−8.7
RD102	2001-08-17	Trib of Da @ Yen Chau	8.01	26.5	41.1	19.6	537	1210	25.7	37.9	3530	150	289	2.072	0.70849	−2.2
RD101	2001-08-17	Da @ Hoa Binh, bl res	7.78	28.3	88.8	26.4	151	508	18.5	32.5	1313	210	122	0.712	0.71207	2.5
RD201	2002-12-27	Da @ Hoa Binh, bl res	7.44	20.2	133	27.7	137	596	35.4	54.2	1603	176	145	1.131	0.71099	−7.4
Thao																
RD131	2001-09-11	Upper Lishe Jiang LB	8.50	20.8	253	58.2	410	924	113	99.0	2594	176	235	1.176	0.71106	2.5
RD229	2003-01-12	Upper Lishe Jiang LB	—	9.6	458	58.7	470	1317	194	199	3812	107	338	1.987	0.71057	−7.7
RD130	2001-09-11	Upper Lishe Jiang RB	8.46	21.3	203	39.5	321	975	62.2	81.9	2646	160	232	1.673	0.71181	−1.3
RD228	2003-01-12	Upper Lishe Jiang RB	—	9.7	489	61.7	340	1321	161	256	3351	145	315	3.015	0.71094	−3.9
RD119	2001-09-05	Red @ Yuan Jiang	8.18	26.0	211	64.4	259	627	70.8	126	1641	166	162	1.257	0.71270	4.1
RD216	2003-01-06	Red @ Yuan Jiang	7.80	16.3	355	56.5	228	617	145	212	1642	167	175	1.823	0.71415	−5.2
RD118	2001-09-05	Huanien He	8.51	27.5	279	42.9	338	914	64.1	210	2369	185	229	2.191	0.71436	−1.0
RD215	2003-01-06	Huanien He	7.70	12.5	245	59.9	166	570	81.9	164	1408	118	145	1.249	0.71647	−2.3
RD106	2001-08-22	Red @ Cua Khao	8.14	27.8	235	56.8	276	669	90.71	141	1801	213	178	1.649	0.71217	1.5
RD205	2002-12-30	Red @ Cua Khao	7.91	16.0	305	37.9	229	892	98.5	193	2031	237	208	2.195	0.71118	2.7
RD117	2001-09-04	Nan Xi	8.41	25.8	87.1	19.7	342	779	12.3	49.8	2253	200	195	0.730	0.71556	−0.7
RD116	2001-09-04	Xiaonan Xi	8.24	25.5	56.4	13.1	417	1170	14	25.5	2910	126	244	0.989	0.71408	8.3
RD107	2001-08-22	Namthe @ Lao Cai	8.38	26.9	71.6	22.7	326	833	14.2	44.8	2335	198	201	0.703	0.71532	−1.1
RD206	2002-12-31	Namthe @ Lao Cai	7.81	15.9	83.8	26.8	394	850	17.4	55.0	2525	180	215	0.816	—	−2.1
RD109	2001-08-23	Red @ Yen Bai	8.14	28.5	226	52.1	237	636	55.4	135	1766	219	173	1.384	0.71242	−3.3
RD208	2002-12-31	Red @ Yen Bai	8.14	15.6	211	38.5	178	647	58.9	128	1587	231	160	1.525	0.71176	−0.1
RD115	2001-08-26	Red @ Phu Tho	8.14	28.4	178	48.4	185	567	71.1	100	1499	210	147	1.158	0.71284	−1.4
RD214	2003-01-02	Red @ Phu Tho	8.25	15.5	206	39.1	175	589	62.0	126	1558	219	155	1.413	0.71206	−5.5
Lo																
RD111	2001-08-24	Lo @ Ha Jiang	8.47	27.3	60.9	23.5	239	991	27.0	69.8	2396	141	208	0.586	0.71161	−0.7
RD211	2003-01-01	Lo @ Ha Jiang	8.45	17.4	43.4	16.0	153	973	22.8	40.1	2283	96.6	192	0.549	0.71137	−3.2
RD112	2001-08-25	Con @ Vinh Tuy	7.75	28.1	48.0	35.1	87.4	276	17.0	19.1	705	150	69.4	0.268	0.71603	6.1
RD212	2003-01-02	Con @ Vinh Tuy	7.77	16.2	92.1	26.6	54.6	276	11.9	12.8	767	218	76.3	0.241	0.72174	−3.1
RD113	2001-08-25	Gam @ Chiem Hoa	8.20	28.9	53.5	24.2	151	842	17.1	32.0	1968	169	172	0.807	0.71111	0.7
RD210	2003-01-01	Gam @ Chiem Hoa	8.28	16.4	56.8	26.4	133	1107	23.9	42.2	2449	143	210	0.886	0.71177	0.2
RD108	2001-08-22	Chay @ Bao Yen	8.24	29.3	70.3	22.3	183	792	14.1	74.2	1936	183	174	0.534	0.71633	−1.8
RD207	2002-12-31	Chay @ Bao Yen	8.05	15.7	94.8	30.5	152	881	20.8	157	1823	198	179	0.586	0.71790	1.5
RD110	2001-08-23	Chay @ Doan Hung	7.72	29.1	58.0	31.8	172	703	18.7	68.2	1671	160	152	—	0.71764	0.7
RD209	2003-01-01	Chay @ Doan Hung	7.90	19.3	91.4	36.7	115	643	22.0	69.3	1556	193	145	0.469	0.71870	−4.4
RD114	2001-08-26	Lo @ Doan Hung, bl Chay	8.18	28.0	56.6	25.7	157	753	29.1	34.5	1796	166	158	0.618	0.71241	1.0
RD213	2003-01-02	Lo @ Doan Hung, bl Chay	8.18	16.5	69.3	29.6	200	960	21	57.8	2139	157	190	0.721	0.71275	5.6

Furthest downstream samples in each tributary system are shaded.

–: no data.

[a] ab = above; bl = below; trib = tributary; LB = left bank; RB = right bank; res = reservoir.

[b] Water temperature.

[c] TDS = total dissolved solid = $Na + K + Mg + Ca + Cl + SO_4 + CO_3 + SiO_2$.

[d] NICB = normalized inorganic charge balance = $(TZ^+ - TZ^-)/TZ^+ \times 100\%$.

Please cite this article in press as: Moon S. et al., Chemical weathering in the Hong (Red) River basin: Rates ..., *Geochim. Cosmochim. Acta* (2007), doi:10.1016/j.gca.2006.12.004

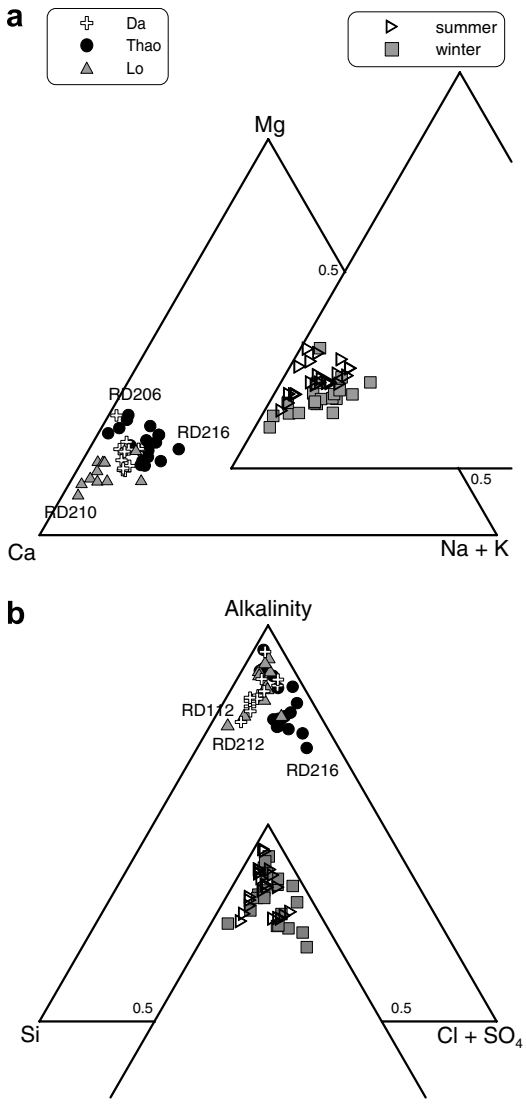

Fig. 3. (a) Cation and (b) anion ternary diagrams (in charge equivalent units). Carbonate weathering (Ca, alkalinity) dominates the major element composition of the Hong. Ca/Mg ratios vary seasonally. The Thao samples show enrichment in $Cl + SO_4$.

ity, also did not show significant correlations with population density. In addition, local rain concentrations (data obtained from EANET: Acid Deposition Monitoring Network in East Asia, Japan, http://www.adorc.gr.jp) accounted for only 5% of riverine TDS, suggesting negligible anthropogenic input of TDS to rivers through atmospheric deposition.

4.3.1. Evaporite dissolution and pyrite oxidation

Halite (NaCl) and gypsum ($CaSO_4{\cdot}2H_2O$)/anhydrite ($CaSO_4$) are the two most common evaporites that can affect river water compositions. The contribution from halite can be estimated in a straightforward manner by assuming that all Cl after correction for atmospheric input (see Section 4.4.1) is from halite. Assessing the contribution from gypsum is complicated, because there are multiple potential sources of dissolved sulfate in rivers.

Sulfate in river water can be supplied by dissolution of gypsum, oxidation of pyrite, pollution, volcanism, rainout of natural biogenic emissions, and cyclic salt, with the first two rock weathering sources being the most important (Berner and Berner, 1996). An assessment can be made of the significance of pyrite oxidation and gypsum dissolution relative to weathering reactions involving carbonic acid by considering the charge balance between $Ca + Mg$ and HCO_3 (alkalinity). Weathering of carbonates or Ca–Mg-silicates by carbonic acid generates equivalent charge units of $Ca + Mg$ and HCO_3. On the other hand, gypsum dissolution and weathering of carbonates or Ca–Mg-silicates by sulfuric acid results in an excess of $Ca + Mg$ over HCO_3. In the Hong samples, $Ca + Mg$ (y-axis) and alkalinity (x-axis) were almost exactly balanced (slope $= 1.001 \pm 0.023$, $r^2 = 0.978$, $p < 0.001$), while both Ca to alkalinity (slope $= 0.723 \pm 0.032$, $r^2 = 0.924$, $p < 0.001$) and $Ca + Mg$ to alkalinity $+ SO_4$ had inferior slopes (slope $= 0.925 \pm 0.029$, $r^2 = 0.962$, $p < 0.001$), suggesting relatively minor contribution from gypsum dissolution or pyrite oxidation compared to carbonic acid mediated reactions.

Distinguishing between the gypsum and pyrite sources of SO_4 is of some concern, because pyrite oxidation generates sulfuric acid, which can be used to weather surrounding carbonate and silicate minerals. Atmospheric CO_2 is not consumed in this process, and thus one can overestimate the drawdown of CO_2 by silicate weathering if neglecting the role of sulfide oxidation.

The alkalinity-Si–($Cl + SO_4$) ternary diagram provides one way to assess the relative importance of gypsum versus pyrite (Fig. 3b). Gypsum dissolution generates data near the ($Cl + SO_4$) apex; pyrite oxidation and accompanying carbonate weathering along the alkalinity-($Cl + SO_4$) axis; and pyrite oxidation with concomitant silicate weathering toward the center of the ternary diagram, because sulfuric acid generates high sulfate, neutralizes the alkalinity, and dissolves silicates. We attempted to quantify this 'uncertainty (H_r)'—the degree of data points to occupy the center of the ternary diagram—using a function similar in form to entropy (Pelto, 1954):

$$100H_r = \frac{-100\sum_{i=1}^{3} p_i \log p_i}{H_m},$$

where the set of probabilities p_1, p_2, and p_3 are calculated from alkalinity, Si, and ($Cl + SO_4$) in charge equivalent units, and H_m is the maximum entropy (1.0986) when $p_1 = p_2 = p_3$. The resulting H_r value is a measure of the relative proportion of sulfate in the sample resulting from sulfide oxidation and silicate weathering. The absolute value of H_r itself does not carry physical meaning, i.e., we cannot anchor the $H_r = 100\%$ to an exact geochemical situation, and this method cannot distinguish between sulfide weathering and mixing of the carbonate–silicate–evaporite end-members. Nevertheless, this offers a semi-quantitative method of estimating the gypsum versus pyrite contributions to dissolved sulfate, which is important for the long-term carbon budget.

The entropy (H_r) in the Hong samples ranged from 25% to 70% (Fig. 6a). A group of relatively high-SO_4 Thao samples had high entropy which suggested that pyrite oxidation

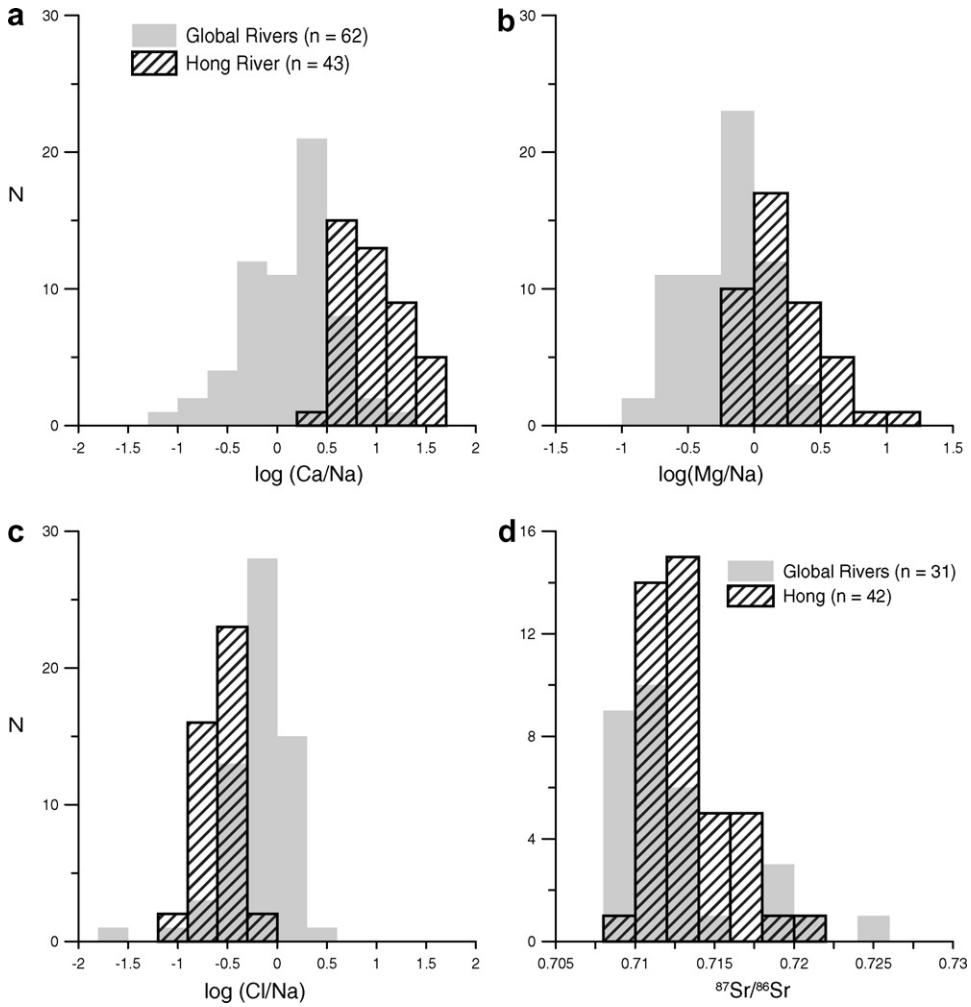

Fig. 4. Histograms of Na-normalized molar ratios—(a) Ca/Na, (b) Mg/Na, (c) Cl/Na—and (d) strontium isotopic ratios of the Hong River samples (this study) and those of Global Rivers (Gaillardet et al., 1999).

was the dominant source of sulfate in these samples. These were the group of samples progressing toward the ($Cl + SO_4$) axis on the ternary diagram (Fig. 3b). They showed a good correlation ($r^2 = 0.916$, $p < 0.001$) between SO_4 and Na^* (Na corrected for rain and halite input and therefore corresponding to the silicate-derived portion), suggesting concomitant weathering of silicates (Fig. 6b). The silicate thus weathered generated cation-rich clays, judging from the relatively low $Si/(Na^* + K)$ ratios (Fig. 6c, see Section 4.3.2). The headwater samples of the Thao (RD228 and 229) had significantly lower entropy compared to other high-SO_4 samples of the Thao (Fig. 6a). While silicate weathering did accompany pyrite oxidation as indicated by the good correlation between SO_4 and Na^*, carbonate weathering exerted an overwhelming influence leading to lower entropy, low Si, and low $^{87}Sr/^{86}Sr$ ratios (Fig. 6b, c, and d). The high dissolved SO_4 observed in the Thao samples and the large contribution from pyrite oxidation is consistent with the known distribution of coal-bearing and sulfide bearing deposits in the area (see Section 2.2). Some of the Da and Lo samples, though their sulfate concentrations were lower, had relatively high contribution from pyrite oxidation relative to gypsum dissolution, judging from their high entropy values, high Si concentrations and $^{87}Sr/^{86}Sr$ ratios (Fig. 6). This is consistent with Galy and France-Lanord (1999), who suggested that 70% of the dissolved sulfate in the Ganges–Brahmaputra is from oxidation of sulfides.

4.3.2. Silicate weathering

The $Si/(Na^* + K)$ ratio is a proxy commonly related to the "intensity" of silicate weathering (Edmond et al., 1995). If K is not from anthropogenic sources, $Na^* + K$ is silicate-derived and accounts for on average 7% of TZ^{+*} ($TZ^+ - Cl$) in our samples, from 1% in RD102 to 14% in RD212. In comparison, it can reach 25% in silicate weathering dominant rivers such as the Yamuna (Dalai et al., 2002). Because the Ca/Na ratio of silicate bedrock in both the Hong and the Yamuna basins were estimated to be ~0.46, this difference in $(Na^* + K)/TZ^{+*}$ is thought to represent lower contribution of silicate weathering to the dissolved load for the Hong samples. The Si–($Na^* + K$) correlation was conspicuous for the Lo samples ($r^2 = 0.983$), while none existed for the Thao or Da (Fig. 6c). The good correlation between $Na^* + K$ and $^{87}Sr/^{86}Sr$ ratios in the Lo samples also supported silicate

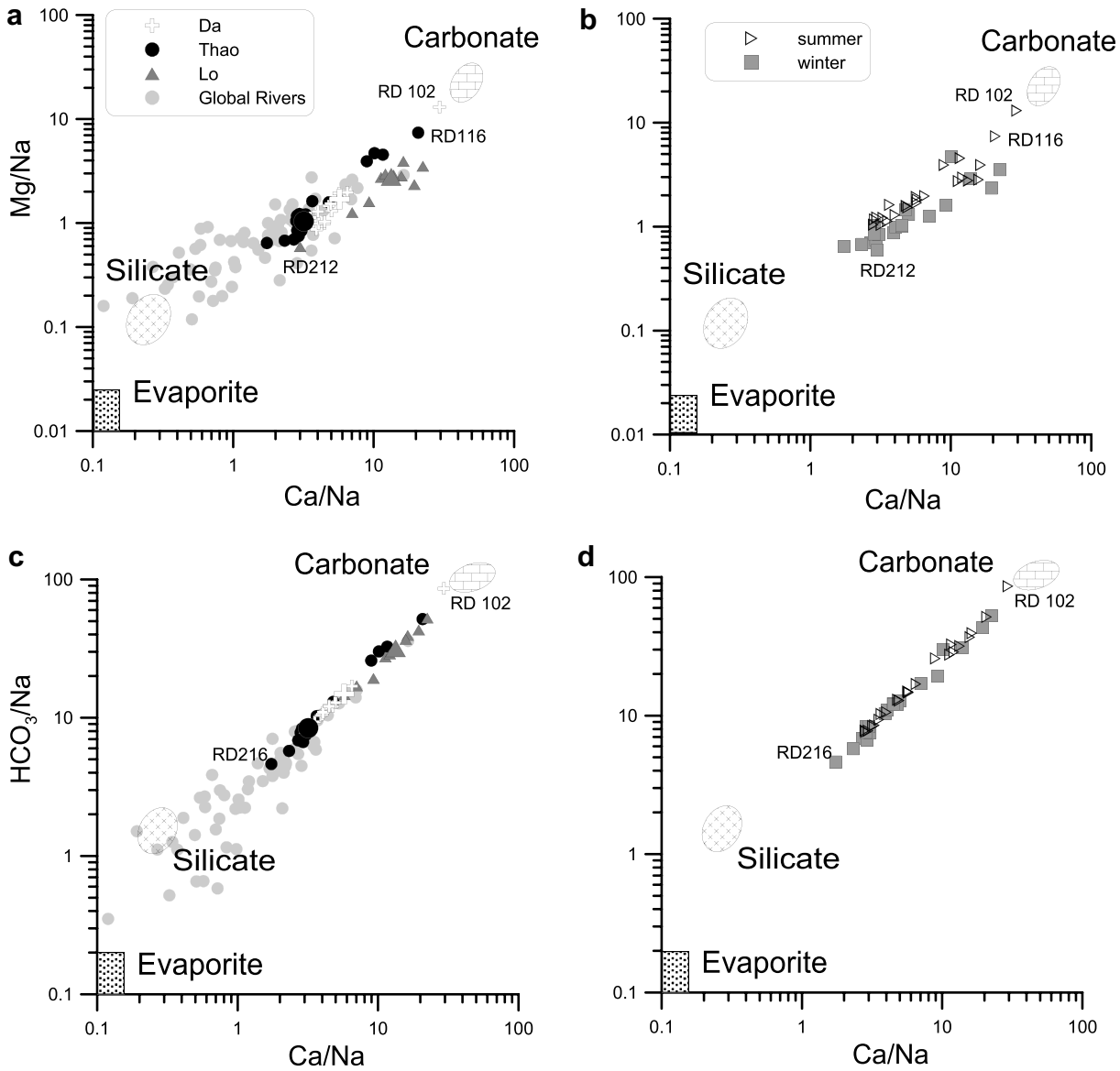

Fig. 5. Mixing diagrams using Na-normalized molar ratios: (a and b) Mg/Na versus Ca/Na (a) by tributary system and (b) by season, and (c and d) HCO_3/Na versus Ca/Na (c) by tributary system and (d) by season. End member compositions of carbonate, silicate, and evaporite are *a posteriori* values of the inverse model (see Section 4.4.4). Enlarged symbols indicate the furthest downstream sample of each tributary system in summer. In (a) and (c), Global Rivers data are plotted in the background for comparison (Gaillardet et al., 1999).

weathering (Fig. 6d). The Si/($Na^* + K$) ratio in the Lo was 2.2 and indicated that silicate weathering proceeded to the kaolinite stage and not completely to the gibbsite stage. For reference, we estimate that weathering of local silicate bedrock to kaolinite and to gibbsite generates Si/($Na^* + K$) ratios of 2 and 3.3, respectively. As explained in Section 4.3.1 sulfuric acid resulting from pyrite oxidation was a supplementary proton source to the carbonic acid ultimately derived from atmospheric CO_2.

4.3.3. Carbonate weathering

Ca and HCO_3^- were the two most abundant ions in the Hong, and 80% of the summer samples (19 of 22 samples) and 44% of the winter samples (8 out of 18 samples) were supersaturated with respect to calcite (Fig. 7). A paired *t*-test showed that the summer samples had higher CSI than winter samples at 0.1% significance level, which we attribute to the effect of higher temperatures. Most of the summer (95%) and winter (72%) samples were similarly supersaturated with respect to dolomite. The Con of the Lo system (RD112, RD 212) is undersaturated with respect to calcite regardless of season. This river had the highest metamorphic rock coverage in the drainage basin (33%), TDS (~75 mg/l, Table 2) lower than the average Global Rivers (~100 mg/l), radiogenic $^{87}Sr/^{86}Sr$ ratios (0.716 in summer and 0.722 in winter), and high Si (~20% of total anions, Fig. 3b). Therefore, underlying lithology appears to exert an important control on the carbonate saturation status of the river.

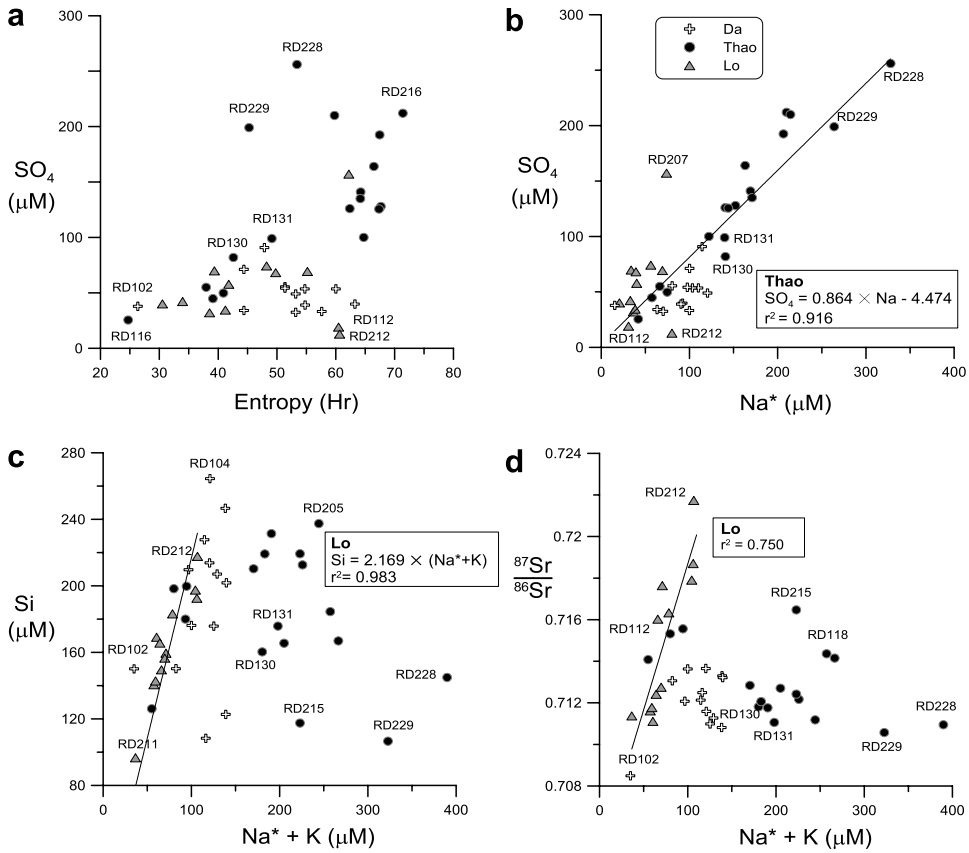

Fig. 6. (a) SO_4 versus entropy (see Section 4.3.1 for definition). (b) SO_4 versus Na^* (Na–Cl) with the least squares fit for the Thao samples. (c) Si versus ($Na^* + K$) and (d) $^{87}Sr/^{86}Sr$ versus ($Na^* + K$) with least squares fit for the Lo samples.

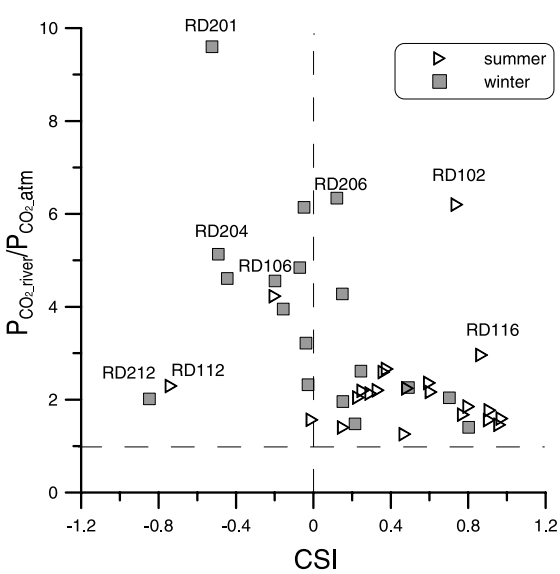

Fig. 7. The CO_2 partial pressure in river water normalized to atmospheric values versus the calcite saturation index ($CSI = \log(\{Ca^{2+}\}\{CO_3^{2-}\}/K_{calcite}$ where {} denotes activity).

We calculated the CO_2 partial pressure (P_{CO_2}) taking into account the effect of elevation (Andrews et al., 1996; Wu et al., 2005):

$$P_z = P_0 \exp(-Z/H),$$

where P_z is the pressure at altitude Z (km), P_0 is CO_2 pressure at sea level (370 μatm); H is the scale height, approximately 8.4 km. P_z was calculated for each sample using average elevation values of the sample drainage basins (Hearn et al., 2001). The Hong was 1–10 times supersaturated (Fig. 7). The photosynthetic productivity and dynamic state of a river determines its P_{CO_2} level (Stallard and Edmond, 1987), and most rivers are up to ~10 times supersaturated with respect to the atmosphere (Huh et al., 1998; Cole and Caraco, 2001; Wu et al., 2005), though tributaries of the Amazon are up to 40 times supersaturated due to root respiration and organic matter decomposition (Stallard and Edmond, 1987; Richey et al., 2002). We attribute the lower P_{CO_2} levels of the Hong in summer to higher photosynthetic activity.

4.3.4. Seasonal variation

A paired-samples t-test on all Hong samples showed that Ca/Mg was lower (Fig. 3a), Mg/TZ^+ was higher, and CSI was also higher (Fig. 7) in summer at the 0.1% significance level ($p < 0.001$). This seasonality was most evident in the Da samples, in which Mg/TZ^+ ratio was positively correlated with CSI ($r^2 = 0.703$, $p = 0.0002$), and Ca/Mg ratio was negatively correlated with CSI ($r^2 = 0.624$, $p = 0.001$), suggesting that the higher temperatures of sum-

mer influenced the carbonate precipitation and exclusion of Mg from its lattice. Additionally, at 1% significance level ($p < 0.01$) for the Da tributary system, $Si/(Na^* + K)$ and $^{87}Sr/^{86}Sr$ were higher in summer, which we interpret as more intensive silicate weathering (see Section 4.3.2). To summarize the seasonal changes, we suspect that in summer carbonate precipitated and more intensive silicate weathering occurred in the Da tributary system.

4.4. Quantification of input sources

To quantify the contributions from rain, evaporite dissolution, carbonate dissolution, and silicate weathering, we used forward and inverse models outlined in Fig. 8.

4.4.1. The forward model

Assuming negligible anthropogenic input, the forward model was based on mass budget equations of cations (Na, Ca, Mg, and K) from four sources—rain, evaporite, carbonate, and silicate (Galy and France-Lanord, 1999; Krishnaswami et al., 1999; Mortatti and Probst, 2003). First, to calculate the input from rain, we assumed that the sample with the lowest Cl content (RD104/RD204 pair) obtained all its Cl (~10 μM) from rain (Table 2). Knowing the cation/Cl ratio of local rain (EANET) (Table 3), we calculated the input of the four cations from rain, which came out to be 1–4% of total dissolved cations. Second, to calculate the input from evaporite, we assumed that excess Cl after rain correction was derived from halite (NaCl). Two limiting cases were considered for SO_4—(i) all sulfate from gypsum dissolution and (ii) all sulfate from pyrite oxidation. Third, to estimate the silicate contribution, all Na after the rain and evaporite corrections and all K after the rain correction were assumed to be from silicate weathering. Ideally, Ca and Mg from silicates should be estimated

Table 3
Inverse model *a posteriori* reservoir compositions to be compared to the *a priori* values in Fig. 8

	Cl/Na	Mg/Na	HCO_3/Na	Ca/Na	Sr/Na	$^{87}Sr/^{86}Sr$
Rain						
Summer	2.15	0.40	0.0001	1.12	0.00019	0.709
Winter	10.50	1.37	0.0001	10.15	0.00019	0.709
Evaporite						
Summer	1	0.02	0.2	0.10	0.005	0.709
Winter	1	0.02	0.3	0.15	0.003	0.709
Silicate						
Summer	0.001	0.09	1.0	0.15	0.0002	0.910
Winter	0.001	0.01	3.0	0.56	0.0002	0.826
Carbonate						
Summer	0.001	18	140	54	0.08	0.709
Winter	0.001	12	91	40	0.07	0.709

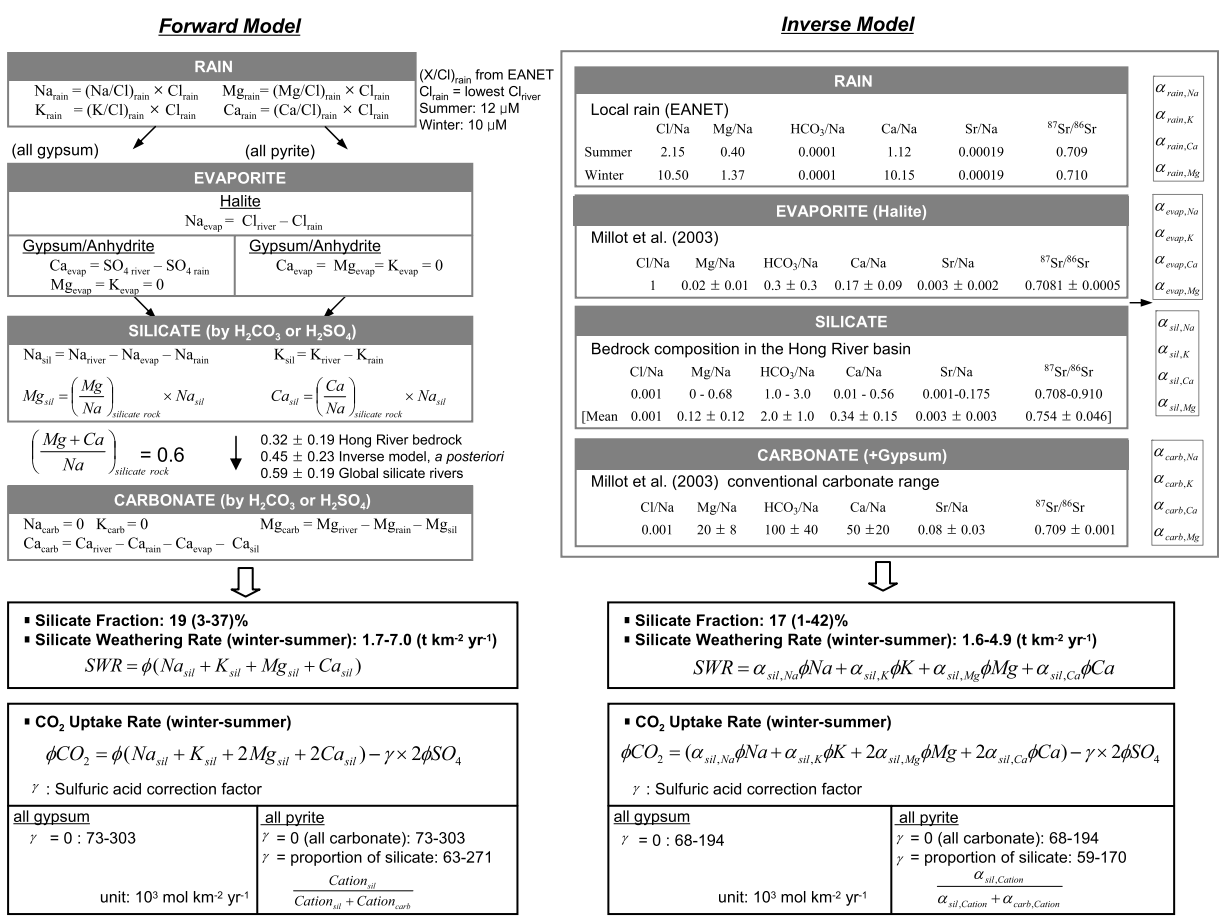

Fig. 8. An outline of the forward and inverse model calculations for the silicate fraction, silicate weathering rate, and rate of CO_2 uptake.

using data from monolithologic streams within the study area. In the absence of appropriate samples, we used $(Ca/Na)_{sil} = 0.44$ and $(Mg/Na)_{sil} = 0.16$ compiled from silicate bedrock data of our study area (Leloup et al., 1995; Zhang and Schärer, 1999; Lan et al., 2000; Roger et al., 2000). The $((Ca + Mg)/Na)_{sil}$ value of 0.6 that we used is a reasonable choice considering that the *a posteriori* values from our inverse model was 0.45 ± 0.23 (see Section 4.4.2), Global Rivers silicate end member composition 0.59 ± 0.19 (Gaillardet et al., 1999), and river waters draining exclusively silicates 0.879 (Boeglin et al., 1997). Fourth, we estimated the input from carbonate weathering by subtracting the rain, evaporite, silicate contributions from the total dissolved Ca and Mg in rivers.

4.4.2. The inverse model

4.4.2.1. Inverse model description. Our inverse model configuration was identical to that of Millot et al. (2003) and detailed explanation about the model used in this paper was presented in Wu et al. (2005). The inverse model was based on a set of mass budget equations of elemental molar ratios (X = Cl, Ca, Mg, HCO_3, and Sr) and Sr isotopic ratios of the four reservoirs (rain, carbonate, silicate, and evaporite) (Négrel et al., 1993). They can be expressed as

$$\left(\frac{X}{Na}\right)_{river} = \sum_i \left(\frac{X}{Na}\right)_i \alpha_{i,Na}$$

$$\left(\frac{^{87}Sr}{^{86}Sr}\right)_{river}\left(\frac{Sr}{Na}\right)_{river} = \sum_i \left(\frac{^{87}Sr}{^{86}Sr}\right)_i \left(\frac{Sr}{Na}\right)_i \alpha_{i,Na}$$

where subscript i indicates the four reservoirs, the $\alpha_{i,Na}$ are the mixing proportions of Na from each reservoir, and $\sum \alpha_{i,Na} = 1$. We excluded SO_4 and K because of non-conservative behavior associated with biological activity (Berner and Berner, 1987) and used Na-normalized ratios and isotopic compositions to remove the effect of discharge and evaporation. We weighted the equations by the analytical error (10% for elemental concentrations and 0.00002 for $^{87}Sr/^{86}Sr$).

We chose a set of *a priori* end member constraints for the reservoirs, $(X/Na)_i$ (Fig. 8): the rain end member was based on seasonally matched local rain (EANET); the carbonate and evaporite end members were from Millot et al. (2003); and the silicate end member was from a compilation of bedrock data in the Hong River basin (Leloup et al., 1995; Zhang and Schärer, 1999; Lan et al., 2000; Roger et al., 2000). Gypsum was included in the carbonate reservoir and pyrite was assumed to be a minor dispersed phase in all rock types. In several sensitivity tests, we varied the composition of the end-members (see Section 4.4.2.2).

Excluding two samples with missing Sr or $^{87}Sr/^{86}Sr$ data, a total of 41 samples (22 summer and 19 winter) were used. Thus, we solved for 179 model parameters ($4i \times 41\alpha_{i,Na} + 15$ $(X/Na)_i$) using 287 equations (6 species × 41 samples = 246 mass balance equations and 41 constraining equations on the sum of fractions) by successive iterations. After we obtained the best $\alpha_{rain,Na}$, $\alpha_{evap,Na}$, $\alpha_{sil,Na}$, and $\alpha_{carb,Na}$ for each sample and the reservoir constraints $(X/Na)_i$, these *a posteriori* values were used to calculate other elemental fractions such as $\alpha_{rain,Ca}$, $\alpha_{evap,Ca}$, $\alpha_{sil,Ca}$, and $\alpha_{carb,Ca}$. The $\alpha_{sil,Cation}$ is the sum of the four cations of silicate origin and is equivalent to $(Na_{sil} + K_{sil} + Ca_{sil} + Mg_{sil})/(Na_{river} + K_{river} + Ca_{river} + Mg_{river})$ calculated in the forward model. The *a posteriori* values for the reservoirs are reported in Table 3. We note that starting from the same *a priori* values for summer and winter, the *a posteriori* values differed seasonally, with the silicate reservoir in summer more radiogenic ($^{87}Sr/^{86}Sr$) and sodic and in winter less radiogenic and calcic (Table 3).

4.4.2.2. Inverse model sensitivity. To assess the sensitivity of the inverse model to the rain end member, we tested 6 scenarios—(1) marine aerosol; local rain compositions of (2) the Qinghai Province (Huang He basin) (Wu et al., 2005) and (3) the Ganges–Brahmaputra basin (Galy et al., 1999); and the local rain of our study area (4) in summer, (5) in winter, and (6) the annual average (EANET) (Table 4). We averaged local rain major element composition of Hoa Binh and Hanoi stations (Fig. 1) for the months of our sampling period and used Sr concentration and isotopic ratios of Galy et al. (1999) and Wu et al. (2005). The inter-scenario differences in the fraction of cations from silicate weathering ($\alpha_{sil,Cation}$) were ~4% (0–10%) and ~6% (1–15%) for $\alpha_{rain,Cation}$. We used seasonally matched local rain compositions (EANET) in our optimized final run.

Another sensitivity test involved three scenarios of varying silicate end member compositions. Other reservoirs (rain, carbonate, and evaporite) and major element composition of the silicate reservoir were held constant, and only the $^{87}Sr/^{86}Sr$ ratio of the silicate reservoir was varied. Scenario #7 had Sr isotopic ratio of 0.720–0.80 from Millot et al. (2003); Scenario #8 had 0.708–0.80 to encompass unradiogenic basalt and volcanic rocks; and in Scenario #9 we explicitly added to Scenario #7 a separate basalt reservoir whose composition was acquired from Das et al. (2005) (0.703–0.709). We used cation fractions without K, because it was difficult to assign specific K compositions to the two reservoirs. Scenarios #7 and #8 produced similar results (~1% difference in $\alpha_{sil,Cation}$; $\alpha_{sil,Cation}$ 1–29%), while the Scenario #9 was ~6 (1–11)% different ($\alpha_{sil,Cation}$ is 1–40 %, 0–21% from radiogenic silicate and 1–19% from unradiogenic silicate). Thus, explicit addition of the unradiogenic silicate reservoir resulted in higher silicate weathering fractions. We do not think Scenario #9 is realistic for the present-day Hong, judging by the major element geochemistry (Section 4.3), but it does provide an upper limit of $\alpha_{sil,Cation}$.

As part of fine-tuning our silicate and rain end member compositions, we ran 4 additional scenarios, this time treating summer and winter samples separately (Scenarios 10–13 of Table 4). In Scenario #10, we assigned a wide range for the silicate reservoir (minimum to maximum in local bedrock) to reflect the diverse type of silicate rocks (Fig. 8). A narrowly defined range based on mean local bedrock value $\pm 1\sigma$ was used in Scenario #11 (Fig. 8). For Scenario #12, a similarly narrow range but outside of the original wide range of Scenario #10 was used. Scenarios #10 and #11 produced similar results (~1% difference in $\alpha_{sil,Cation}$), while Scenario #12 is ~11 (0–24)% different (Table 4). We conclude that for the Hong data set, the inverse model can produce robust results even when the end member com-

Table 4
Silicate fraction ($\alpha_{sil,Cation}$) from inverse model sensitivity tests

Sample No.	Rain[a]						Silicate[b]				Seasonal[c]				Forward model
	(1)	(2)	(3)	(4)	(5)	(6)	(7)	(8)	(9a)	(9b)	(**10**)	(11)	(12)	(13)	
Da															
RD120	13	12	13	13	16	15	11	10	9	8	**13**	12	22	—	17
RD217	14	13	14	15	17	17	12	12	10	8	**19**	20	30	19	20
RD121	12	11	12	12	15	14	10	10	9	8	**12**	11	16	—	14
RD218	14	13	14	15	18	17	13	13	11	10	**20**	22	35	20	15
RD105	19	18	20	21	24	23	17	17	14	11	**19**	18	42	—	25
RD203	18	17	18	19	22	21	16	16	13	10	**25**	24	37	24	26
RD104	19	18	19	20	20	21	15	15	11	8	**18**	17	37	—	27
RD204	18	18	18	19	19	19	15	15	10	7	**21**	21	31	21	28
RD103	15	15	16	16	18	18	13	12	10	8	**15**	14	31	—	22
RD202	17	16	17	17	19	19	14	14	10	7	**21**	20	32	21	25
RD102	1	1	1	1	1	1	0	0	0	1	**1**	1	1	—	3
RD101	13	13	13	14	16	16	10	10	8	7	**14**	13	22		19
RD201	15	14	15	15	18	17	12	12	10	7	**19**	18	28	18	22
Thao															
RD131	19	18	19	20	23	22	16	16	14	13	**18**	16	14	—	18
RD229	21	20	21	23	26	25	18	19	16	13	**28**	30	38	27	21
RD130	13	13	13	14	16	16	11	11	9	8	**13**	12	21	—	18
RD228	20	19	20	21	25	24	17	18	15	10	**23**	23	33	23	27
RD119	21	20	21	22	25	24	16	16	14	10	**20**	18	29	—	26
RD216	26	26	26	27	31	31	22	23	20	11	**26**	27	47	26	32
RD118	17	16	17	18	20	20	15	14	12	8	**16**	15	33	—	25
RD215	25	24	25	26	30	29	20	20	17	11	**29**	29	49	29	32
RD106	20	19	20	21	24	23	16	16	13	9	**18**	17	34	—	27
RD205	18	18	18	19	22	22	16	16	14	9	**19**	19	32	19	26
RD117	10	10	10	11	12	12	9	8	6	8	**10**	9	24	—	12
RD116	4	3	4	4	5	4	3	3	2	4	**4**	3	5	—	5
RD107	8	8	8	8	10	10	6	6	5	7	**8**	7	15	—	10
RD109	21	20	21	22	25	25	17	17	14	10	**20**	19	36	—	29
RD208	19	18	19	20	23	22	16	16	13	9	**22**	21	33	21	27
RD115	19	19	20	21	24	23	15	15	13	9	**18**	17	30		26
RD214	19	19	20	21	24	23	16	16	14	9	**22**	22	34	22	28
Lo															
RD111	7	7	7	7	8	8	5	5	5	6	**6**	6	6	—	7
RD211	5	5	5	5	6	5	3	3	3	5	**8**	8	13	7	5
RD112	19	18	19	20	22	21	12	12	11	11	**19**	17	21	—	21
RD212	33	31	35	37	41	39	29	28	21	19	**42**	39	51	41	37
RD113	6	6	6	6	7	7	4	4	3	4	**6**	6	9	—	8
RD210	5	5	5	5	6	6	3	3	3	4	**8**	8	11	8	7
RD108	10	9	10	10	12	11	8	8	6	8	**10**	9	21	—	11
RD207	12	12	12	13	15	14	10	10	8	9	**19**	18	29	18	14
RD209	16	15	16	17	20	19	12	12	11	11	**23**	22	46	23	18
RD114	8	7	8	8	9	9	5	5	5	6	**8**	7	10	—	10
RD213	7	7	7	8	9	9	5	5	4	7	**11**	12	18	11	8

Furthest downstream samples in each tributary system are shaded, and column in bold indicates our final choice.

[a] Sensitivity test for the rain end member (1) marine aerosol (2) Qinghai Province (3) Ganges–Brahmaputra basin (4) local summer (5) local winter (6) annual mean (see text for data sources).

[b] Sensitivity test for the silicate end member by changing $^{87}Sr/^{86}Sr$: (7) 0.72–0.80, (8) 0.708–0.80; (9a) felsic silicate 0.72–0.80 (9b) mafic silicate 0.703–0.709 (molar fraction without K).

[c] Sensitivity test considering seasonality (10) local min–max (11) local mean $\pm 1\sigma$ (12) within #10, outside #11 (13) 3 year-averaged winter rain.

positions are given large ranges. However, narrowly defined end member compositions, if wrong, can produce spurious results. Thus, we consider the wider range of Scenario #10 a better choice.

Scenario #13 was a further test of our rain end member. The local rain (EANET) in winter (Hoa Binh station in January 2003) had unusually high Cl/Na and Ca/Na, and there was concern that this was spurious data. So for Scenario #13 we used the 3-yr mean excluding the 2003 data, such that Cl/Na = 3.74, Ca/Na = 4.00, and Mg/Na = 0.53 (cf. Fig. 8). The difference between the Scenarios #10 and #13 for $\alpha_{sil,Cation}$ was ~2% (1–4%) and for $\alpha_{rain,Cat-}$

$_{ion}$ was ~1% (0–4%). Because we do not have a convincing reason to reject the questionable 2003 winter data, we retained Scenario #10 as our best estimate.

Our sensitivity tests indicated that blind use of the inverse model can be problematic (5 (0–11)% difference in $\alpha_{sil,Cation}$ between the 9 scenarios) (Table 4). However, with background information on the end-members this uncertainty can be narrowed and one can arrive at relatively robust results.

4.4.3. Model results

According to the forward model assuming all sulfate was from gypsum, rain contributed 2 (1–4)%, evaporite 8 (0–26)%, carbonate 71 (41–94)%, and silicate 19 (3–37)% to the total dissolved cations on molar basis. Assuming all sulfate from pyrite gave 2 (1–4)% from rain, 2 (0–11)% from evaporite, 77 (56–95)% from carbonate, and 19 (3–37)% from silicate. The differences between the two limiting cases were in higher evaporite in the all-gypsum case and higher carbonate contributions in the all-pyrite case; silicate fraction was calculated independently of the limiting assumptions. According to the inverse model, rain was 2 (0.0–8)%, evaporite 3 (0.2–13)%, carbonate 78 (55–97)%, and silicate 17 (1–42)% of total dissolved cations on a molar basis (Table 5 and Fig. 9). This was in broad agreement with the all-pyrite case of the forward model. The propagated uncertainties for $\alpha_{i,Cation}$ of the 4 reservoirs—rain, evaporite, carbonate, and silicate—were ±0.5%, 0.5%, 11%, and 1%, respectively. The high uncertainty for the carbonates was due to its high values (>70%). For both models, the highest evaporite contribution was in sample RD216, highest carbonate and lowest silicate contributions in RD102, and the lowest carbonate and highest silicate contributions in RD212 (also see Figs. 3, 5–7).

Table 5
Results from forward and inverse models for the Hong River

Sample No.	Area (10^3 km^2)	Discharge[a] (km^3/yr)	Source of cation[b] (mol %)				Dissolved flux of cations (10^9mol/yr)			SWR (tons/km^2/yr)		SWR (10^3 mol/km^2/yr)			ϕ CO_2 (10^3 mol/km^2/yr)		TDS yield (10^6 mol/km^2/yr)
			Rain	Evaporite	Carbonate	Silicate	Evaporite	Carbonate	Silicate	Inverse	Forward	Inverse	Forward	2ϕSi	Inverse	Forward	
(A) Winter																	
Da																	
RD217	3.664	0.975	2	2	77	19	0.02	0.83	0.20	**1.7**	1.7	**55.9**	57.7	65.3	**65.8**	67.4	0.859
RD218	5.600	1.81	7	2	71	20	0.04	1.56	0.45	**2.5**	1.7	**79.5**	59.9	69.9	**101**	73.3	1.11
RD203	26.36	8.00	2	2	72	25	0.14	4.97	1.70	**2.0**	2.0	**64.4**	67.1	122	**79.2**	82.6	0.805
RD204	6.537	1.62	0	2	77	21	0.02	0.94	0.26	**1.2**	1.6	**39.5**	52.9	122	**43.1**	62.7	0.588
RD202	43.47	13.8	0	2	77	21	0.21	8.43	2.29	**1.6**	1.9	**52.7**	63.6	131	**60.9**	76.0	0.800
RD201	51.06	16.0	1	4	77	19	0.51	11.0	2.67	**1.6**	1.8	**52.3**	60.5	110	**61.1**	72.7	0.865
Thao																	
RD229	0.890	0.299	8	3	62	28	0.02	0.42	0.19	**6.4**	4.8	**213**	165	71.7	**244**	189	2.22
RD228	1.634	0.503	1	8	68	23	0.09	0.76	0.26	**4.8**	5.3	**159**	184	89.3	**166**	200	1.89
RD216	20.76	4.41	1	13	60	26	0.74	3.31	1.45	**2.1**	2.5	**69.9**	85.3	70.8	**60.8**	80.4	0.726
RD215	2.400	0.185	2	7	62	29	0.01	0.12	0.06	**0.7**	0.8	**23.4**	25.5	18.1	**21.7**	24.7	0.217
RD205	34.09	6.40	0	9	72	19	0.83	6.73	1.81	**1.6**	2.1	**53.2**	71.0	89.2	**53.0**	75.1	0.756
RD206	4.011	0.959	—	—	—	—	—	—	—	—	1.0	—	34.1	86.1	—	41.9	0.988
RD208	44.69	9.78	0	6	72	22	0.69	7.75	2.34	**1.6**	1.9	**52.3**	65.7	104	**53.0**	70.7	0.674
RD214	48.42	11.3	1	7	70	22	0.77	7.97	2.55	**1.6**	1.9	**52.8**	64.9	102	**52.6**	68.8	0.692
Lo																	
RD211	7.133	1.67	5	1	87	8	0.01	1.72	0.16	**0.8**	0.4	**22.1**	13.7	45.3	**32.0**	16.8	0.851
RD212	1.234	0.499	1	3	55	42	0.01	0.12	0.09	**2.5**	2.0	**76.3**	66.5	176	**105**	84.0	0.590
RD210	15.06	5.08	2	1	89	8	0.06	5.97	0.52	**1.2**	1.0	**34.4**	29.8	96.3	**46.2**	36.2	1.34
RD207	4.305	1.61	3	1	78	19	0.02	1.45	0.35	**2.7**	1.8	**80.8**	59.3	148	**98.4**	61.3	1.26
RD209	6.302	2.37	4	1	72	23	0.03	1.50	0.49	**2.6**	1.8	**77.5**	59.0	145	**100**	67.0	1.02
RD213	36.30	12.1	4	1	84	11	0.13	12.7	1.72	**1.6**	1.1	**47.3**	34.5	104	**63.6**	40.8	1.21
(B) Summer																	
Da																	
RD120	3.664	4.60	2	1	84	13	0.04	3.54	0.55	**4.1**	5.7	**150**	197	443	**156**	238	3.43
RD121	5.600	7.78	4	1	84	12	0.04	5.92	0.84	**4.2**	5.3	**151**	180	418	**167**	224	3.77
RD105	26.36	37.5	3	2	76	19	0.51	21.4	5.47	**5.6**	7.8	**208**	269	608	**223**	334	3.17
RD104	6.537	8.59	0	2	80	18	0.11	4.69	1.08	**4.6**	7.2	**166**	243	695	**166**	292	2.77
RD103	43.47	67.4	1	1	82	15	0.83	45.5	8.47	**5.4**	8.1	**195**	275	706	**204**	338	3.83
RD102	0.834	1.24	1	0	97	1	0.01	2.19	0.03	**1.2**	2.5	**30.6**	78.8	447	**29.6**	94.8	8.27
RD101	51.06	79.6	1	2	84	14	1.07	51.6	8.37	**4.7**	6.8	**164**	230	654	**172**	282	3.66
Thao																	
RD131	0.890	1.16	8	1	73	18	0.01	1.39	0.34	**10.6**	11.3	**378**	377	456	**395**	442	6.01
RD130	1.63	1.87	1	3	82	13	0.10	2.37	0.37	**6.3**	9.2	**227**	313	367	**234**	379	5.14
RD119	20.76	20.4	1	6	73	20	1.37	17.4	4.64	**6.5**	8.8	**224**	293	325	**202**	312	3.11
RD118	2.400	1.23	0	5	79	16	0.10	1.52	0.31	**3.5**	5.9	**128**	202	189	**107**	214	2.25
RD106	34.09	31.3	0	7	75	18	2.68	29.0	6.95	**5.8**	9.2	**204**	309	391	**178**	331	3.18
RD117	3.16	3.47	1	0	89	10	0.01	3.78	0.41	**3.7**	4.7	**130**	163	439	**150**	203	4.11
RD116	0.275	0.421	1	0	95	4	0.002	0.66	0.03	**2.8**	4.0	**95.8**	136	386	**115**	176	7.24
RD107	4.011	4.85	2	0	90	8	0.02	5.48	0.49	**3.5**	4.4	**121**	149	479	**140**	184	4.65
RD109	44.69	48.6	0	6	4	20	3.12	41.2	11.4	**7.1**	10.7	**254**	363	477	**224**	389	3.62
RD115	48.42	54.7	1	6	5	18	3.45	40.0	9.76	**5.8**	8.5	**202**	285	476	**183**	310	3.22
Lo																	
RD111	7.133	8.80	4	0	90	6	0.03	10.4	0.73	**3.1**	3.3	**102**	107	347	**115**	125	4.87
RD112	1.234	2.45	5	0	76	19	0.004	0.83	0.20	**5.2**	5.9	**165**	185	594	**173**	213	2.65
RD113	15.06	27.8	1	1	92	6	0.21	1.83	.8	**3.7**	5.1	**121**	168	624	**132**	205	6.01
RD108	4.305	7.56	2	0	88	10	0.02	7.18	0.78	**5.3**	6.3	**181**	212	643	**199**	248	5.77
RD110	6.302	11.4	—	—	—	—	—	—	—	—	5.8	—	186	575	—	209	5.19
RD114	36.30	63.2	2	0	89	8	0.24	56.0	4.93	**4.1**	5.1	**136**	167	576	**150**	202	5.23

Furthest downstream samples in each tributary system are shaded, and column in bold indicates our final choice.

[a] Discharge = runnoff X drainage area.

[b] Acquired from the inverse model.

We examined the inter-tributary differences in the fraction of cations from silicate ($\alpha_{sil,Cation}$) by comparing only the summer samples—14% for the Da, 18% for the Thao, 8% for the Lo. A summer–winter paired-samples *t*-test gave higher silicate contribution in winter for all three model results at the 5% significance level, possibly because the weathering yield of carbonates is about 4 times more sensitive to runoff than that of silicates at high runoff (Tipper et al., 2006).

Paired samples *t*-test indicated that the forward and inverse model results for $\alpha_{sil,Cation}$ have a significant correlation ($r^2 = 0.756$, $p < 0.001$), and the difference between the two models is less than 9% (average ~3%). We favor the inverse model results, because the forward model results are highly dependent on the assumed $((Ca + Mg)/Na)_{sil}$ value (Fig. 8). Since the three rivers displayed different silicate weathering patterns (Fig. 6), we back-calculated the $((Ca + Mg)/Na)_{sil}$ values for the three tributary systems such that the forward and inverse model results for $\alpha_{sil,Cation}$ agreed. The values differed greatly—0.4 for the Da, 0.3 for the Thao, and 1 for the Lo. While we use $((Ca + Mg)/Na)_{sil}$ value of 0.6 for all samples, the back calculation provided a measure of potential variation and associated uncertainty in the forward model.

4.5. Flux calculations

The total dissolved solid (TDS, defined in Table 2) yield was on the order of 10^6 mol/km^2/yr in most samples; 1 (0.2–2.2) $\times 10^6$ mol/km^2/yr in winter and 5.6 (2.3–8.3) $\times 10^6$ mol/km^2/yr in summer (Table 5). To compare to other global rivers, we recalculated the TDS yield using summer samples and annual average discharge—1.5 (0.7–3.1) $\times 10^6$ mol/km^2/yr. This value was comparable to other Himalayas-Tibetan Plateau rivers (Upper Huang He: 0.56–1.5, Ganges–Brahmaputra: 1.7–5.7, and Indus: 1.3 $\times 10^6$ mol/km^2/yr) (Galy et al., 1999; Karim and Veizer, 2000; Dalai et al., 2003; Wu et al., 2005) as well as other rivers draining orogenic zones such as the Amazon (0.59–4.1) $\times 10^6$ mol/km^2/yr and Mackenzie (0.5–4.9) $\times 10^6$ mol/km^2/yr, but higher than the Orinoco (0.96–1.6) $\times 10^6$ mol/km^2/yr draining the Andes, or rivers of the Russian Far East draining the collision zone (0.04–0.38) $\times 10^6$ mol/km^2/yr (Stallard and Edmond, 1983; Edmond et al., 1996; Huh et al., 1998; Galy and France-Lanord, 1999). In comparison, rivers draining shield terrains have low TDS yield—e.g., the Amazon draining the Brazilian Shield 0.3 $\times 10^6$ mol/km^2/yr, Orinoco draining the Guayana Shield (0.01–0.6) $\times 10^6$ mol/km^2/yr, St. Lawrence draining the Canadian Shield (0.04-0.07) $\times 10^6$ mol/km^2/yr, or the rivers draining the Siberian Shield (0.09–1.5 $\times 10^6$ mol/km^2/yr) (Edmond et al., 1995; Gaillardet et al., 1997; Huh and Edmond, 1999; Millot et al., 2003).

Assuming that the density of rock is 2.7 g/cm^3, we calculated the chemical denudation rate in the Red River basin from the TDS yield of the furthest downstream samples of the 3 tributary systems: ~0.08 mm/yr in summer and ~0.02 mm/yr in winter. We estimated the physical denudation rate using suspended particulate sediment yield. The SPM content of the Hong was 139 mg/L in summer and 69 mg/L in winter (Table 6), but these values are probably underestimates, since this estimate was based on the furthest downstream samples of the Da (RD101/201) and the Lo (RD114/213) located below reservoirs. Using samples above reservoirs, the estimated SPM increased to 343 mg/L in summer and 111 mg/L in winter. Physical denudation rates calculated from the SPM were ~0.18 mm/yr in summer and ~0.01 mm/yr in winter. Total denudation rates, sum of chemical and physical denudation rates, were 0.25 mm/yr in summer and 0.03 mm/yr in winter. We note that in summer physical denudation was ~70% of the total denudation, whereas in winter chemical denudation was slightly higher (~40:60) (Table 6). The 9-fold increase in total denudation rate from winter to sum-

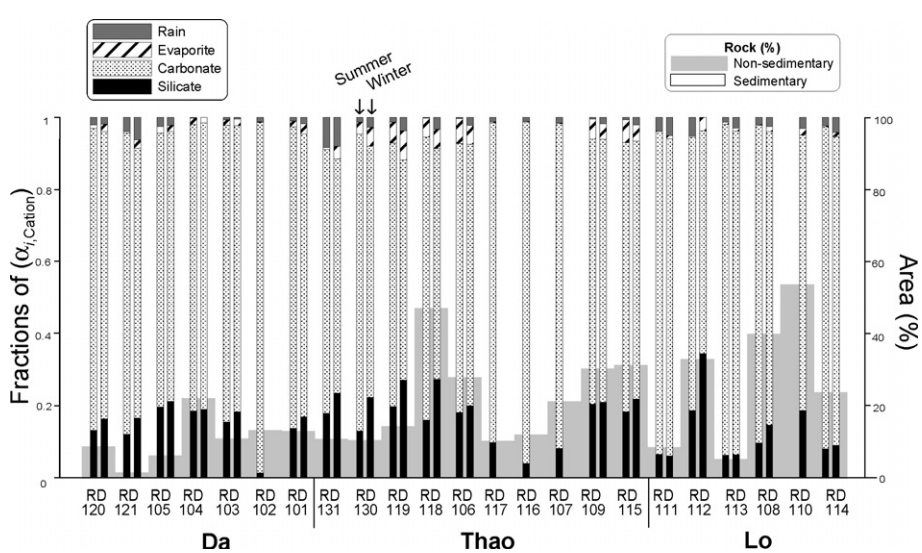

Fig. 9. Fraction of total dissolved cations ($\alpha_{i,Cation} = \alpha_{i,Na} + \alpha_{i,K} + \alpha_{i,Mg} + \alpha_{i,Ca}$) from rain, evaporite, carbonate, and silicate in summer (left bar) and in winter (right bar). Generally, the silicate-derived fraction was higher in winter. The shaded background is percentage of drainage basin area covered by non-sedimentary (i.e., igneous and metamorphic) rocks.

Table 6
Denudation rates of the Hong River

Sample No.	SPM[a] (mg/L)	Denudation rates (mm yr^{-1}) Physical	Chemical	Total
Da				
RD101	70.2	0.041	0.071	0.111
RD103	531	0.305	0.074	0.379
RD201	3.3	0.0004	0.017	0.017
RD202	89.0	0.010	0.016	0.026
Thao				
RD115	261	0.109	0.062	0.171
RD214	155	0.013	0.013	0.027
Lo				
RD114	45.7	0.029	0.102	0.131
RD113	66.5	0.045	0.117	0.163
RD213	37.7	0.005	0.024	0.028
RD210	35.4	0.004	0.026	0.031
Hong River				
Summer	343	0.180	0.074	0.254
Winter	111	0.011	0.016	0.027

[a] SPM: suspended particulate material estimated by weighing material collected on filters. Mean density for rock is 2.7 g/cm^3.

mer was primarily due to the 16-fold increase in the physical denudation rate.

The total denudation rate in the Hong basin is comparable to the average Neogene exhumation rates calculated by fission track (0.104–0.191 mm/yr) and to the estimate from Pleistocene sediment volumes in the Hong River basin (0.178 mm/yr) (Clift et al., 2006). Total denudation rate in the Hong is much lower than maximum total denudation rates in the eastern and western syntaxes of the Himalayas—10 mm/yr for the Namche Barwa determined by fission track (Burg et al., 1998) and 3–5 mm/yr for the Nanga Parbat calculated from mineral cooling ages (Moore and England, 2001). This is probably due to the exceptional focused erosion in the syntaxes of the Himalayas.

The silicate weathering rate (SWR) was calculated as the sum of cations from weathering of silicate by either carbonic acid or sulfuric acid (Table 5 and Fig. 8):

$$\mathrm{SWR_{forward}} = \phi(\mathrm{Na_{sil}} + \mathrm{K_{sil}} + \mathrm{Mg_{sil}} + \mathrm{Ca_{sil}})$$
$$\mathrm{SWR_{inverse}} = \alpha_{\mathrm{sil,Na}}\phi\mathrm{Na_{river}} + \alpha_{\mathrm{sil,K}}\phi\mathrm{K_{river}} + \alpha_{\mathrm{sil,Mg}}\phi\mathrm{Mg_{river}} + \alpha_{\mathrm{sil,Ca}}\phi\mathrm{Ca_{river}}$$

where ϕ indicates yield (mol/km^2/yr). Our best estimate of the SWR for the Hong River is an area weighted average of the furthest downstream samples of the three tributaries calculated with the inverse model: 51 (22–213) $\times 10^3$ mol/km^2/yr in winter and 170 (31–378) $\times 10^3$ mol/km^2/yr in summer. Thus, the SWR was ~3 times higher in summer due to higher water discharge. The propagated uncertainty for SWR is ~40% from the ~30% uncertainty on both the $\alpha_{\mathrm{sil,Cation}}$ and the water discharge. Forward model results gave similar SWR for winter, 55 (14–184) $\times 10^3$ mol/km^2/yr, but higher for summer, 233 (79–377) $\times 10^3$ mol/km^2/yr. The highest SWR was observed in the headwaters of the Thao (RD130/228, 131/229) for both seasons and lowest SWR in the small carbonate tributary of the Lo (RD102, no winter sample). While the Con River (RD212) of the Lo system had the highest silicate fraction, owing to the low cation concentrations its SWR was not as high.

A simplistic method of calculating SWR is by assuming that the sole source of dissolved Si is weathering of silicates. Potential involvement of Si with the biogeochemical cycle within the water body is discounted, and a general relationship between SWR and flux of Si is assumed (SWR = 2ϕSi) (Edmond and Huh, 1997). For the Hong, the area-weighted averages were 106 (20–180) $\times 10^3$ mol/km^2/yr in winter and 570 (190–710) $\times 10^3$ mol/km^2/yr in summer. These values were on average 2.2 times higher than the inverse model results. This discrepancy arose because the SWR = 2ϕSi relationship was originally derived from rivers draining igneous or metamorphic rocks whose Si/HCO_3^- was 0.3–0.5 (Garrels, 1967), whereas our samples had much lower ratios of Si/HCO_3^- (0.03–0.28). The inverse model results showed better correlation with the forward model ($r^2 = 0.899$) than with the silica-based method ($r^2 = 0.365$, $p < 0.001$).

The uptake of atmospheric CO_2 by silicate weathering is dependent on how the sulfate in rivers is accounted for—gypsum dissolution versus pyrite oxidation—and in the latter case, on how much of the sulfuric acid was used to weather silicates versus carbonates (Fig. 8). In the limiting case of all sulfate supplied from gypsum dissolution, ϕCO_2 is equal to the SWR. In the second limiting case of all sulfate supplied from pyrite oxidation, sulfuric-acid mediated, non-CO_2 consuming silicate weathering has to be subtracted. In charge-equivalent form, it can be expressed as:

$$\phi\mathrm{CO_{2_{forward}}} = \phi(\mathrm{Na_{sil}} + \mathrm{K_{sil}} + 2\mathrm{Mg_{sil}} + 2\mathrm{Ca_{sil}}) - \gamma \times 2\phi\mathrm{SO_{4river}}$$
$$\phi\mathrm{CO_{2_{inverse}}} = (\alpha_{\mathrm{sil,Na}}\phi\mathrm{Na_{river}} + \alpha_{\mathrm{sil,K}}\phi\mathrm{K_{river}} + 2\alpha_{\mathrm{sil,Mg}}\phi\mathrm{Mg_{river}} + 2\alpha_{\mathrm{sil,Ca}}\phi\mathrm{Ca_{river}}) - \gamma \times 2\phi\mathrm{SO_{4river}}$$

where γ is an adjustment factor for sulfuric acid which can vary from 0 to 1. If all sulfuric acid is consumed in weathering carbonates ($\gamma = 0$), ϕCO_2 = SWR = 68 (30–286) $\times 10^3$ mol/km^2/yr in winter and 194 (31–445) $\times 10^3$ mol/km^2/yr for summer, equivalent to the all-gypsum case above. If all sulfuric acid is consumed in weathering silicates ($\gamma = 1$), ϕCO_2 values of some tributary samples came out to be negative numbers, an obviously unrealistic situation. To fine-tune the proportion of carbonate versus silicate weathered by the sulfuric acid, we made use of the carbonate: silicate contributions (in charge equivalent units) to the total dissolved cations calculated in Section 4.4.3 (Table 5), in which case the ϕCO_2 was 59 (22–244) $\times 10^3$ mol/km^2/yr for winter and 170 (30–395) $\times 10^3$ mol/km^2/yr for summer. The ϕCO_2 was ~3 times higher in summer. The assumed value of γ made on average only about 15% difference in ϕCO_2 and indicates that the major proton donor in the Hong River system is carbonic acid and that sulfuric acid plays only a minor role. The results for equivalent calculation using the forward model were similar for the winter and 30–50% higher for the summer, and the values are reported in Fig. 8.

The Hong has similar net ϕCO_2 compared to the HTP Rivers and other orogenic rivers, the Amazon and Orinoco, $\sim(100–570) \times 10^3$ mol/km^2/yr (Wu et al., 2005), but higher than rivers draining shields—e.g., the Amazon draining the Brazilian Shield 58×10^3 mol/km^2/yr, Orinoco draining the Guayana Shield 102×10^3 mol/km^2/yr, St. Lawrence draining the Canadian Shield $(5–11) \times 10^3$ mol/km^2/yr, or the rivers draining the Siberian Shield $(21 \times 10^6$ mol/km^2/yr). The CO_2 consumption rate of shield region is calculated from the same forward model as ours (Edmond et al., 1995; Gaillardet et al., 1997; Huh and Edmond, 1999; Millot et al., 2003).

4.6. Factors controlling the CO_2 consumption rate

Multiple co-dependent factors—geologic (elevation, relief, slope, and lithology) and climatic (temperature, precipitation, potential evapotranspiration, and runoff)—influence the chemical weathering processes (West et al., 2005). We took advantage of the geographic information systems (GIS) to quantify the above parameters for each sample basin and tested for statistical correlations with ϕCO_2. We excluded 5 outlier samples—the headwaters of the Thao (RD228/130, 229/131) with extremely high silicate weathering rates and sulfate concentrations and a small tributary of the Da (RD102) which has an exclusively carbonate composition—and treated the summer and winter samples separately. Correlation coefficient (r^2) greater than 0.25, significant at 5% level, was only obtained for ϕCO_2 with runoff ($r^2 = 0.624$) and with relief ($r^2 = 0.252$) in winter samples and with precipitation ($r^2 = 0.252$) for summer samples. Better correlations with climatic parameters can be obtained if summer and winter samples are treated together. However, that is a spurious result in that the "climate" is not the climatic regime sustained for extended periods of time nor the large range covered by tropical and polar drainage basins. One reason for the lack of clear correlations with climatic/geologic parameters is that the relative magnitude of physical and chemical weathering differs seasonally. In winter, chemical weathering is a significant factor and the dependence of silicate weathering rates and hence ϕCO_2 on parameters like runoff and relief are expected to be more conspicuous. On the other hand, in summer episodic flood events are responsible for the high physical weathering. In the latter case, the amount of precipitation and mobilization of SPM can be an important effect. At a more fundamental level, we cannot rigorously correlate factors involving different inherent time scales—i.e., climatic data (runoff, precipitation, potential evapotranspiration, and temperature) are averaged over several years, geologic data (relief, slope, and exposed rock type) respond to much longer time scales, but the silicate weathering rates calculated from dissolved river load are "instantaneous".

5. CONCLUSIONS

This paper focuses on the aqueous geochemistry of the Hong (Red) River and chemical weathering rate calculations. We have extensively tested both the forward and inverse models and find that for rivers in a geologically complex setting, correct identification of the reservoirs involved and their chemical compositions is a critical and most difficult step. The Hong dissolved load originated predominantly from carbonate (55–97%) rather than silicate (1–40%) weathering. Although the 3 main tributary systems of the Hong are geographically juxtaposed, their dissolved chemical compositions differed: carbonate and silicate weathering with minor rain and halite input adequately explained the Lo data, but additional pyrite oxidation accompanied by Na-silicates weathering occurred in the Thao and the Da. Our best estimate of the silicate weathering rates in the Hong basin was 51 (winter) to 170 (summer) $\times 10^3$ mol/km^2/yr, and ascertaining the source of the sulfate in the rivers did not prove critical, because carbonic acid was the major agent of weathering. GIS treatment yielded poor correlation between rates of CO_2 uptake and climatic/geologic factors, suggesting that chemical weathering of silicates is a complex function involving multiple parameters.

ACKNOWLEDGMENTS

The authors thank A. Ellis, L. Wu, H. Noh, and J. Borges for valuable discussions and for the group effort in maintaining the lab. We also thank T. Bullen of USGS for access to TIMS, T. K. Dalai, J. Gaillardet, two anonymous reviewers, and the associate editor S. Krishnaswami for their constructive comments. This study was supported by US NSF EAR 0134966 and SNU Startup funds to Y. Huh, and the Brain Korea 21 graduate student fellowship to S. Moon.

REFERENCES

Andrews J. E., Brimblecombe P., Jickells T. D., and Liss P. S. (1996) *An Introduction to Environmental Chemistry*. Blackwell, Oxford.

Berner E. K., and Berner R. A. (1987) *The Global Water Cycle Geochemistry and Environment*. Prentice-Hall, Englewood Cliffs, NJ.

Berner E. K., and Berner R. A. (1996) *Global Envoironment: Water, Air, and Geochemical Cycles*. Prentice-Hall, Englewood Cliffs, NJ.

Berner R. A. (1991) A model for atmospheric CO_2 over Phanerozoic times. *Am. J. Sci.* **291**, 339–376.

Bethke C. M. (2002) *The Geochemist's Workbench 4.0*. University of Illinois, USA.

Bickle M. J., Chapman H. J., Bunbury J., Harris N. B. W., Fairchild I. J., Ahmad T., and Pomiès C. (2005) Relative contributions of silicate and carbonate rocks to riverine Sr fluxes in the headwaters of the Ganges. *Geochim. Cosmochim. Acta* **69**(9), 2221–2240.

Boeglin J.-L., Mortatti J., and Tardy Y. (1997) Chemical and mechanical erosion in the upper Niger basin (Guinea, Mali). Geochemical weathering budget in tropical environment. *Compt. Rendus Geosci.* **325**(3), 185–191.

Burchfiel B. C., and Wang E. (2003) Northwest-trending, middle Cenozoic, left-lateral faults in southern Yunnan, China, and their tectonic significance. *J. Struct. Geol.* **25**(5), 781–792.

Burg J.-P., Nievergelt P., Oberli F., Seward D., Davy P., Maurin J.-, Diao Z., and Meier M. (1998) The Namche Barwa syntaxis: evidence for exhumation related to compressional crustal folding. *J. Asian Earth Sci.* **16**(2–3), 239–252.

Burke W. H., Denison R. E., Hetherington E. A., Koepnick R. B., Nelson H. F., and Otto J. B. (1982) Variation of seawater $^{87}Sr/^{86}Sr$ throughout Phanerozoic time. *Geology* **10**(10), 516–519.

Center for International Earth Science Information Network (CIESIN), Columbia University; International Food Policy Research Institute (IFPRI); The World Bank; and Centro Internacional de Agricultura Tropical (CIAT). (2004) Global Rural-Urban Mapping Project (GRUMP), Alpha Version. Palisades, NY: Socioeconomic Data and Applications Center (SEDAC), Columbia University. Available at <http://sedac.ciesin.columbia.edu/gpw/>. Accessed June 1, 2006.

Clift P. D., Carter A., Campbell I. H., Pringle M. S., Lap N. V., Allen C. M., Hodges K. V., and Tan M. T. (2006) Thermochronology of mineral grains in the Red and Mekong Rivers, Vietnam: provenance and exhumation implications for Southeast Asia. *Geochem. Geophys. Geosyst.* **7**.

Cole J. J., and Caraco N. F. (2001) Carbon in catchments: connecting terrestrial carbon losses with aquatic metabolism. *Mar. Freshwat. Res.* **52**(1), 101–110.

Dalai T. K., Krishnaswami S., and Kumar A. (2003) Sr and $^{87}Sr/^{86}Sr$ in the Yamuna River System in the Himalaya: sources, fluxes, and controls on Sr isotope composition. *Geochim. Cosmochim. Acta* **67**(16), 2931–2948.

Dalai T. K., Krishnaswami S., and Sarin M. M. (2002) Major ion chemistry in the headwaters of the Yamuna river system: chemical weathering, its temperature dependence and CO_2 consumption in the Himalaya. *Geochim. Cosmochim. Acta* **66**(19), 3397–3416.

Das A., Krishnaswami S., Sarin M. M., and Pande K. (2005) Chemical weathering in the Krishna Basin and Western Ghats of the Deccan Traps, India: Rates of basalt weathering and their controls. *Geochim. Cosmochim. Acta* **69**(8), 2067–2084.

Dosseto A., Bourdon B., Gaillardet J., Allègre C. J., and Filizola (2006) Time scale and conditions of weathering under tropical climate: Study of the Amazon basin with U-series. *Geochim. Cosmochim. Acta* **70**(1), 71–89.

Edmond J. M. (1992) Himalayan tectonics, weathering processes and the strontium isotope record in marine limestones. *Science* **258**, 1594–1597.

Edmond J. M., and Huh Y. (1997) Chemical weathering yields from basement and orogenic terrains in hot and cold climates. In *Tectonic Uplift and Climate Change*, (ed. W.F. Ruddiman), pp. 329–351. Plenum Press, Englewood Cliffs, NJ.

Edmond J. M., Palmer M. R., Measures C. I., Brown E. T., and Huh Y. (1996) Fluvial geochemistry of the eastern slope of the northeastern Andes and its foredeep in the drainage of the Orinoco in Colombia and Venezuela. *Geochim. Cosmochim. Acta* **60**(16), 2949–2974.

Edmond J. M., Palmer M. R., Measures C. I., Grant B., and Stallard R. F. (1995) The fluvial geochemistry and denudation rate of the Guayana Shield in Venezuela, Colombia, and Brazil. *Geochim. Cosmochim. Acta* **59**(16), 3301–3325.

Fekete B. M., Vörösmarty C. J., and Grabs W. (2002) High-resolution fields of global runoff combining observed river discharge and simulated water balances. *Global Biogeochem. Cycles* **16**(3).

Gaillardet J., Dupré B., and Allègre C. J. (1995) A global geochemical mass budget applied to the Congo basin rivers: erosion rates and continental crust composition. *Geochim. Cosmochim. Acta* **59**(17), 3469–3485.

Gaillardet J., Dupré B., Allègre C. J., and Négrel P. (1997) Chemical and physical denudation in the Amazon River Basin. *Chem. Geol.* **142**(3-4), 141–173.

Gaillardet J., Dupré B., Louvat P., and Allègre C. J. (1999) Global silicate weathering and CO_2 consumption rates deduced from the chemistry of large rivers. *Chem. Geol.* **159**(1–4), 3–30.

Galy A., and France-Lanord C. (1999) Weathering processes in the Ganges–Brahmaputra basin and the riverine alkalinity budget. *Chem. Geol.* **159**(1-4), 31–60.

Galy A., France-Lanord C., and Derry L. A. (1999) The strontium isotopic budget of Himalayan rivers in Nepal and Bangladesh. *Geochim. Cosmochim. Acta* **63**(13–14), 1905–1925.

Garrels R. M. (1967) Genesis of some groundwaters from igneous rocks. In *Researches in Geochemistry*, (ed. P.H. Abelson). , vol. 2, pp. 405–420. John Wiley & Sons, New york.

Hearn P., Hare T., Schruben P., Sherrill D., Lamar C., and Tsushima P. (2001) *Global GIS Database: Digital Atlas of South Asia*. U.S. Geological Survey.

Huh Y., and Edmond J. M. (1999) The fluvial geochemistry of the rivers of Eastern Siberia: III. Tributaries of the Lena and Anabar draining the basement terrain of the Siberian Craton and the Trans-Baikal Highlands. *Geochim. Cosmochim. Acta* **63**(7–8), 967–987.

Huh Y., Panteleyev G., Babich D., Zaitsev A., and Edmond J. M. (1998) The fluvial geochemistry of the rivers of Eastern Siberia: II. Tributaries of the Lena, Omoloy, Yana, Indigirka, Kolyma, and Anadyr draining the collisional/accretionary zone of the Verkhoyansk and Cherskiy ranges. *Geochim. Cosmochim. Acta* **62**(12), 2053–2075.

Karim A., and Veizer J. (2000) Weathering processes in the Indus River Basin: implications from riverine carbon, sulfur, oxygen, and strontium isotopes. *Chem. Geol.* **170**(1–4), 153–177.

Krishnaswami S., Singh S. K., and Dalai T. K. (1999) Silicate weathering in the Himalaya: role in contributing to major ions and radiogenic Sr to the Bay of Bengal. In *Ocean Science, Trends and Future Directions*, (ed. B.L.K. Somayajulu), pp. 23–51. Indian National Science Academy and Akademia International.

Lan C.-Y., Chung S.-L., Lo C.-H., Lee T.-Y., Wang P.-L., Li H., and Toan V. D. (2001) First evidence for Archean continental crust in northern Vietnam and its implications for crustal and tectonic evolution in Southeast Asia. *Geology* **29**(3), 219–222.

Lan C.-Y., Chung S.-L., Shen J. J.-S., Lo C.-H., Wang P.-L., Hoa T. T., Thanh H. H., and Mertzman S. A. (2000) Geochemical and Sr–Nd isotopic characteristics of granitic rocks from northern Vietnam. *J. Asian Earth Sci.* **18**(3), 267–280.

Leemans R. and Cramer W. (1991) The IIASA database for mean monthly values of temperature, precipitation and cloudiness on a global terrestrial grid. IIASA Research Report RR-91-18. International Institute of Applied Systems Analyses, pp. 61.

Leloup P. H., Lacassin R., Tapponnier P., Schärer U., Zhong D., Liu X., Zhang L., Ji S., and Trinh P. T. (1995) The Ailao Shan-Red River shear zone (Yunnan, China), Tertiary transform boundary of Indochina. *Tectonophysics* **251**(1–4), 3–10.

Mathers S. J., Davies J., McDonald A., Zalasiewicz J. A., and Marsh S. (1997) The Red River Delta of Vietnam. British Geological Survey Technical Report WC/96/02.

Mathers S. J., and Zalasiewicz J. A. (1999) Holocene sedimentary architecture of the Red River delta, Vietnam. *J. Coast. Res.* **15**, 314–325.

Meybeck M., and Ragu A. (1997) *River Discharges to the Oceans: An Assessment of Suspended Solids, Major Ions and Nutrients*. UNEP Publication.

Millot R., Gaillardet J., Dupré B., and Allègre C. J. (2003) Northern latitude chemical weathering rates: clues from the Mackenzie River Basin, Canada. *Geochim. Cosmochim. Acta* **67**(7), 1305–1329.

Moore M. A., and England P. C. (2001) On the inference of denudation rates from cooling ages of minerals. *Earth Planet. Sci. Lett.* **185**(3–4), 265–284.

Mortatti J., and Probst J.-L. (2003) Silicate rock weathering and atmospheric/soil CO_2 uptake in the Amazon basin estimated

from river water geochemistry: seasonal and spatial variations. *Chem. Geol.* **197**(1–4), 177–196.

Négrel P., Allègre C. J., Dupré B., and Lewin E. (1993) Erosion sources determined by inversion of major and trace element ratios and strontium isotopic ratios in river: the Congo Basin case. *Earth Planet. Sci. Lett.* **120**(1–2), 59–76.

Pelto C. R. (1954) Mapping of multicomponent systems. *J. Geol.* **62**(5), 501–511.

Penn J. R. (2001) Rivers of the World: A Social, Geographical, and Environmental Sourcebook ABC-CLIO.

Raymo M. E., and Ruddiman W. F. (1992) Tectonic forcing of late Cenozoic climate. *Nature* **359**(6391), 117–122.

Richey J. E., Melack J. M., Aufdenkampe A. K., Ballester V. M., and Hess L. L. (2002) Outgassing from Amazonian rivers and wetlands as a large tropical source of atmospheric CO_2. *Nature* **416**(6881), 617–620.

Roger F., Leloup P. H., Jolivet M., Lacassin R., Trinh P. T., Brunel M., and Seward D. (2000) Long and complex thermal history of the Song Chay metamorphic dome (Northern Vietnam) by multi-system geochronology. *Tectonophysics* **321**(4), 449–466.

Schärer U., Tapponnier P., Lacassin R., Leloup P. H., Zhong D., and Ji S. (1990) Intraplate tectonics in Asia: a precise age for large-scale Miocene movement along the Ailao Shan-Red River shear zone, China. *Earth Planet. Sci. Lett.* **97**(1–2), 65–77.

Stallard R. F., and Edmond J. M. (1983) Geochemistry of the Amazon 2. The influence of geology and weathering environment on the dissolved load. *J. Geophys. Res.* **88**(C14), 9671–9688.

Stallard R. F., and Edmond J. M. (1987) Geochemistry of the Amazon. 3. Weathering chemistry and limits to dissolved inputs. *J. Geophys. Res.* **92**(C8), 8293–8302.

Tipper E. T., Bickle M. J., Galy A., West A. J., Pomiès C., and Chapman H. J. (2006) The short term climatic sensitivity of carbonate and silicate weathering fluxes: insight from seasonal variations in river chemistry. *Geochim. Cosmochim. Acta* **70**(11), 2737–2754.

Wakita K., Okubo Y., Bandibas J. C., Lei X., Schulte M., J. D., and CCOP-DCGM phase I Working Group. (2004) Digital Geologic Map of East and Southeast Asia. In Digital Geoscience Map G-2 Geological Survey of Japan, AIST.

Walker J. C. G., Hays P. B., and Kasting J. F. (1981) A negative feedback mechanism for the long-term stabilization of Earth's surface temperature. *J. Geophys. Res.* **86**, 9776–9782.

Wang C. Y., Zhou M.-F., and Zhao D. (2005) Mineral chemistry of chromite from the Permian Jinbaoshan Pt–Pd–sulphide-bearing ultramafic intrusion in SW China with petrogenetic implications. *Lithos* **83**(1–2), 47–66.

West A. J., Galy A., and Bickle M. (2005) Tectonic and climatic controls on silicate weathering. *Earth Planet. Sci. Lett.* **235**(1–2), 211–228.

Wolf A. T., Natharius J. A., Danielson J. J., Ward B. S., and Pender J. K. (1999) International river basins of the world. *Int. J. Water Resour. Dev.* **15**(4), 387–427.

World Wildlife Fund. (2000) World Wildlife Fund Ecoregions. In ESRI Data & Maps Environmental Systems Research Institute, Inc. (ESRI).

Wu L., Huh Y., Qin J., Du G., and van Der Lee S. (2005) Chemical weathering in the Upper Huang He (Yellow River) draining the eastern Qinghai-Tibet Plateau. *Geochim. Cosmochim. Acta* **69**(22), 5279–5294.

Wysocka A., and Swierczewska A. (2003) Alluvial deposits from the strike-slip fault Lo River Basin (Oligocene/Miocene), Red River Fault Zone, north-western Vietnam. *J. Asian Earth Sci.* **21**(10), 1097–1112.

Zhang L.-S., and Schärer U. (1999) Age and origin of magmatism along the Cenozoic Red River shear belt, China. *Contrib. Mineral. Petrol.* **134**(1), 67–85.

Associate editor: S. Krishnaswami

Please cite this article in press as: Moon S. et al., Chemical weathering in the Hong (Red) River basin: Rates ..., *Geochim. Cosmochim. Acta* (2007), doi:10.1016/j.gca.2006.12.004